Report Title	**A Data Fusion System for the Nondestructive Evaluation of Non-Piggable Pipes**
Type of Report	Final Report
Reporting Period Start Date	October 1, 2002
Reporting Period End Date	March 31, 2005
Principal Author(s)	Dr. Shreekanth Mandayam (PI), Dr. Robi Polikar (Co-PI), Dr. John C. Chen (Co-PI)
Date Report was Issued	February 2006
DOE Award Number	**DE-FC26-02NT41648**
Name and Address of the Submitting Organization	Rowan University 201 Mullica Hill Road Glassboro, NJ 08028

Disclaimer

"This report was prepared as an account of work sponsored by an agency of the United States Government. Neither the United States Government nor any agency thereof, nor any of their employees, makes any warranty, express or implied, or assumes any legal liability or responsibility for the accuracy, completeness, or usefulness of any information, apparatus, product, or process disclosed, or represents that its use would not infringe privately owned rights. Reference herein to any specific commercial product, process, or service by trade name, trademark, manufacturer, or otherwise does not necessarily constitute or imply its endorsement, recommendation, or favoring by the United States Government or any agency thereof. The views and opinions of authors expressed herein do not necessarily state or reflect those of the United States Government or any agency thereof."

Abstract

The objectives of this research project are –

1. To design sensor data fusion algorithms that can synergistically combine defect related information from heterogeneous sensors used in gas pipeline inspection for reliably and accurately predicting the condition of the pipe-wall.
2. To develop efficient data management techniques for signals obtained during multisensor interrogation of a gas pipeline.

This final report summarizes all research activities conducted by Rowan University during the project period. This includes the design and development of experimental validation test platforms, the design and development of data fusion algorithms for defect identification and sizing, and finally, the design and development of advanced visualization algorithms for the effective management of data resulting from multi-sensor interrogation of gas transmission pipelines.

Table of Contents

List of Graphical Material

Executive Summary

The objectives of this research project are:

1. To design sensor data fusion algorithms that can synergistically combine defect related information from heterogeneous sensors used in gas pipeline inspection for reliably and accurately predicting the condition of the pipe-wall.
2. To develop efficient data management techniques for signals obtained during multisensor interrogation of a gas pipeline.

The principal research activities and contributions are listed below:

1. Fabrication of test specimen suites for performing NDE in the laboratory: The first test specimen suite consists of 4" x 6" ASTM-836 steel specimens with simulated benign and anomalous indications in the range of 0.01" – 0.03" and pipe-wall thicknesses 5/16" – 1/2". These were used for magnetic, thermal and ultrasonic imaging. The second test specimen suite consists of 0.5" thick SA-516-Grade-70 steel coupons containing simulated cracks of varying depths of 0.08", 0.16", and 0.32" – these were subjected to bi-axial loads and used for acoustic and ultrasonic imaging (*Subtask 4.1 – Specimen Fabrication*).
2. Design and development of a test platform for performing multi-sensor NDE of test specimens under bi-axial load simulating the conditions inside a pressurized pipe. (*Subtask 4.2 – Test Platform Development*).
3. Obtaining magnetic flux leakage (MFL), ultrasonic testing (UT), thermal imaging and acoustic emission (AE) data from test specimens. (*Subtask 4.3 – Obtain Multisensor NDE Data*).
4. Design and development of a neural-network based geometric transformation algorithm for extracting redundant and complementary information present among NDE signatures obtained using different inspection methods. (*Subtask 3.1 – Development of measures for complementarity and redundancy of information in fused signals*).
5. Design and development of an incremental machine learning algorithm for fusing data from multiple inspection modalities to identify and separate pipe-wall anomalies from benign indications. (*Subtask 3.2 – Development of algorithms for defect identification*)
6. The demonstration of the algorithms ability to fuse data from multiple homogeneous and heterogeneous sensors: Redundant and complementary information related to the location and size of a pipe-wall defect was predicted using homogeneous data combinations that include UT-MFL, UT-thermal imaging and MFL-thermal imaging; the heterogeneous data combination includes UT-AE. The heterogeneous data was pre-processed using a Parzen windows technique to generate an equivalent homogeneous data set, before being fused with other homogeneous data (*Subtask 3.3 – Development of algorithms for defect sizing*).
7. Development of a framework for multi-sensor data visualization in a virtual reality (VR) platform: An immersive, interactive and navigable VR data fusion environment was defined and created, consisting of (a) graphical data, (b) measurement data, and (c) functional data. The framework was demonstrated using multi-sensor data obtained during the in-line inspection of a section of a gas transmission pipeline. Graphical models

of the pipeline components were displayed in addition to MFL / UT inspection signals, neural network predictions of pipeline condition, and the geographic location of the pipeline network. (*Task 5.0 – Recommendations for Effective Data Management*)

8. Research and development partnerships: Rowan University has established a research partnership with RTD Quality Services, USA based out of Houston, Texas and through their contacts with TransCanada Pipelines. The objective of this partnership is to gain access to field pipeline inspection data and arrive techniques for field-validation of the multi-sensor data fusion algorithms that have been developed as part of this project.
9. Results from this research activity formed the basis of the following MS Theses published by Rowan University:
    a. Joseph Oagaro, Master of Science, Electrical Engineering, Thesis: *Heterogeneous Multi-Sensor Data Fusion Using Geometric Transformations And Parzen Windows For The Nondestructive Evaluation Of Gas Transmission Pipelines,* Dec 2004.
    b. Scott Papson, Master of Science, Electrical Engineering, Thesis: *An Investigation Of Multi-Dimensional Evolutionary Algorithms For Virtual Reality Scenario Development,* May 2004.
    c. Philip J. Kulick, Master of Science, Electrical Engineering, Thesis: *Multi-Sensor Data Fusion Using Geometric Transformations For The Nondestructive Evaluation Of Gas Transmission Pipelines,* Dec 2003.

    They were also presented and published in the proceedings of the *Sensors in Industry Conference* in New Orleans (January 2004), *Natural Gas Technologies II* Conference in Phoenix (February 2004), *Review of Progress in Quantitative Nondestructive Evaluation (QNDE)* conference in Golden, Colorado (July 2004).

Experimental

The experimental aspect of this research work was divided into the following tasks and subtasks:

Task 3.0 *Design and Development of Data Fusion Algorithms*

Subtask 3.1 Development of measures for complementarity and redundancy of information in fused signals

Subtask 3.2 Development of algorithms for defect identification

Subtask 3.3 Development of algorithms for defect sizing

Task 4.0 *Design and Development of the Validation Test Platform*

Subtask 4.1 Specimen fabrication

Subtask 4.2 Test platform development

Subtask 4.3 Obtain multisensor NDE signals

Task 5.0 *Recommendations for Effective Data Management*

Chronologically, however, the project activities began with Task 4.0 since the test platform and NDE signals were required to perform the data fusion in Task 3.0. Research progress in each of the tasks and subtasks is described in the following sections.

Task 4.0 – Design and Development of the Validation Test Platform

Subtask 4.1 – Specimen fabrication

The research team fabricated of two suites of test specimens that would provide a diversity of NDE data when subjected to multi-sensor interrogation. The first suite of test specimens provide two specific types of NDE signatures – benign indications and anomalies. The benign indications that were selected included pipe-welds and straps. Anomalies included pitting corrosion, narrow cracks indicative of SCC and gouges/dents indicative of mechanical damage. ASTM 836 steel stock was purchased for fabricating these specimens in thicknesses of $^{5}/_{16}$, $^{3}/_{8}$ and $^{1}/_{2}$ inch.

All of the specimens have length and width dimensions of 6” x 4” and can be viewed in Figure 1. Three specimens, one of each thickness, have been fabricated with no defect as shown in Figure 1(a). Figure 1(b) displays one of the specimens developed to mimic pitting corrosion defects. A total of nine slotted defect specimens were produced in a milling machine with 0.1”,

0.2” and 0.3” defect depths for all three specimen thicknesses discussed earlier. The suite also contains one specimen of each thickness with crack, gouge/dent and weld defects. Figure 1(c) shows the specimen simulating stress corrosion cracking by producing a saw cut in the center of the specimen with a depth of 80% of the overall thickness. The specimens with gouges/dents were produced using a hydraulic press to cause mechanical damage of the specimens. The welds were produced by machining two pieces of steel that were half the size of the original specimen size and welding the pieces together at the midline. Finally the specimens with straps were produced by welding an external strip of metal over the spliced specimen to join the two pieces. These specimens can be viewed in Figure 1(d), 1(e), and 1(f) respectively. All of the specimens are numerically identified and outlined in Table 1.

(a) No defect **(b) Slotted defect**

Figure 1: Test specimen suite.

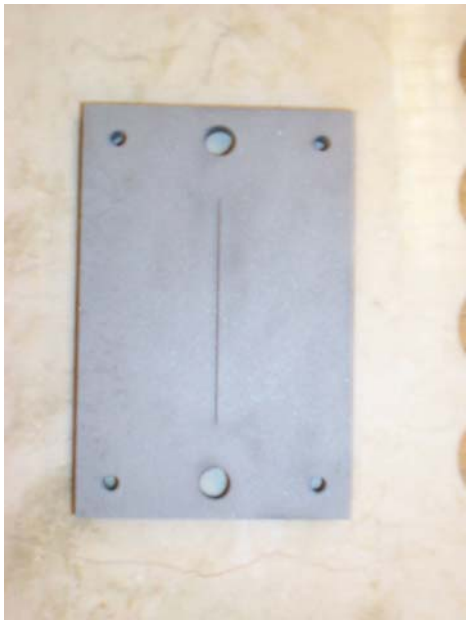

(c) Saw cut defect

(d) Mechanical damage defect

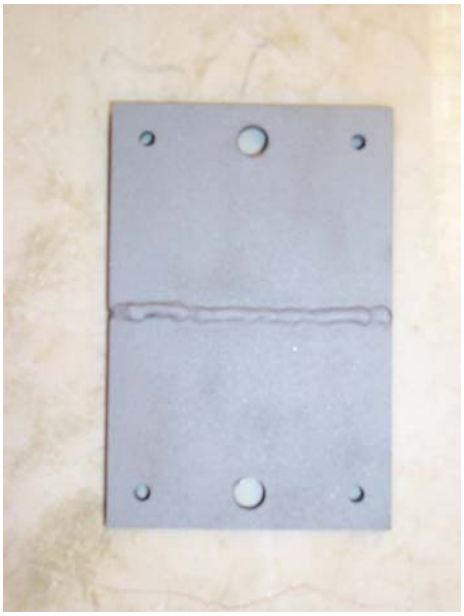

(e) Weld defect

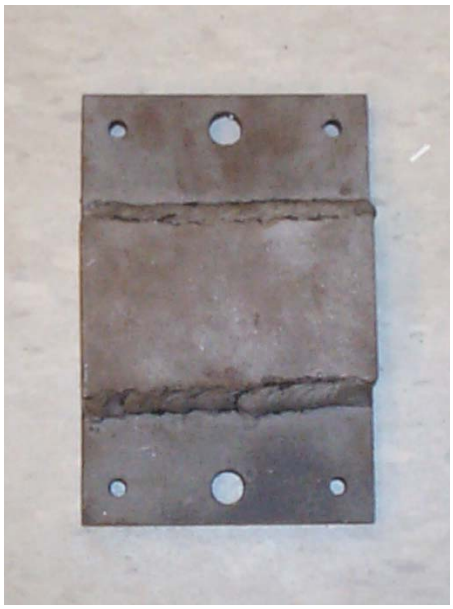

(f) Strap Defect

Figure 1: Test specimen suite (continued).

Table 1: Details of the test specimens in the suite.

Specimen #	Plate thickness (in)	Indication Type	Depth (in)
00	0.5	None	N/A
01	0.5	Pitting	0.3005
02	0.5	Pitting	0.198
03	0.5	Pitting	0.0945
04	0.5	Crack	80% Sawcut
05	0.5	Mechanical Damage	Varies
06	0.5	Weld	Varies
07	0.5	Strap	Varies
10	0.375	None	N/A
11	0.375	Pitting	0.298
12	0.375	Pitting	0.199
13	0.375	Pitting	0.1105
14	0.375	Crack	80% Sawcut
15	0.375	Mechanical Damage	Varies
16	0.375	Weld	Varies
17	0.375	Strap	Varies
20	0.3125	None	N/A
21	0.3125	Pitting	0.303
22	0.3125	Pitting	0.1955
23	0.3125	Pitting	0.0995
24	0.3125	Crack	80% Sawcut
25	0.3125	Mechanical Damage	Varies
26	0.3125	Weld	Varies
27	0.3125	Strap	Varies
Note: All specimens have a length of 6 inches and a width of 4 inches.			

The second suite test specimens consist of 0.5” thick SA-516-Gr. 70 steel coupons as shown in Figure 2 (a). A set of six specimens containing simulated cracks of varying depth (0.08”, 0.16”, and 0.32”) was obtained from Shell in October 2002. In order to assist in the test platform development process and to conduct initial tests, identically dimensioned specimens were fabricated in the Rowan Waterjet machining center, shown in Figure 2 (b). The material used for fabricating the in-house test specimens is ASTM 836 mild steel. These specimens all contained 80% deep, 2.5” long saw-cut simulated cracks.

Figure 2: (a) Test specimens provided by Shell, (b) fabricated in-house.

Subtask 4.2 – Test Platform Development

The Acoustic Emission (AE) test platform allows for biaxial loading of test-specimens in order to simulate axial and hoop stresses in a pressurized gas pipeline – the design is illustrated in Figure 3. It uses a set of four (4) A-572 grade 50 steel blocks referred to as specimen-clamping brackets. The brackets are used in connecting the specimens to the loading mechanism and load transducers of the test platform. Each specimen-clamping bracket is joined to the specimen with a 1" diameter pin to allow for pivoting of the specimen during testing.

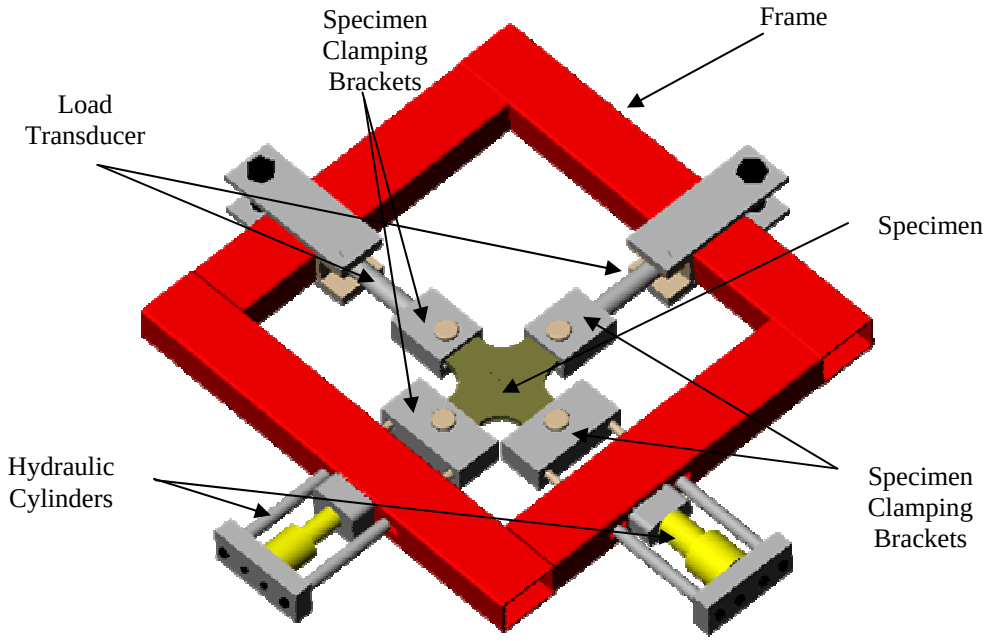

Figure 3: AE test platform.

The test platform is shown fully assembled in Figure 4. The addition of hydraulic loading cylinders will allow for the maximum desired load of 30 ksi to be placed on the specimens in the biaxial direction. This also provides for uniform testing to be performed in a controlled loading situation. The hydraulics consist of Enerpac RC-Series single acting cylinders with 15 & 25 ton capacities. A 10,000 psi hand pump will be employed to reach a required full load of 45,000 lbs.

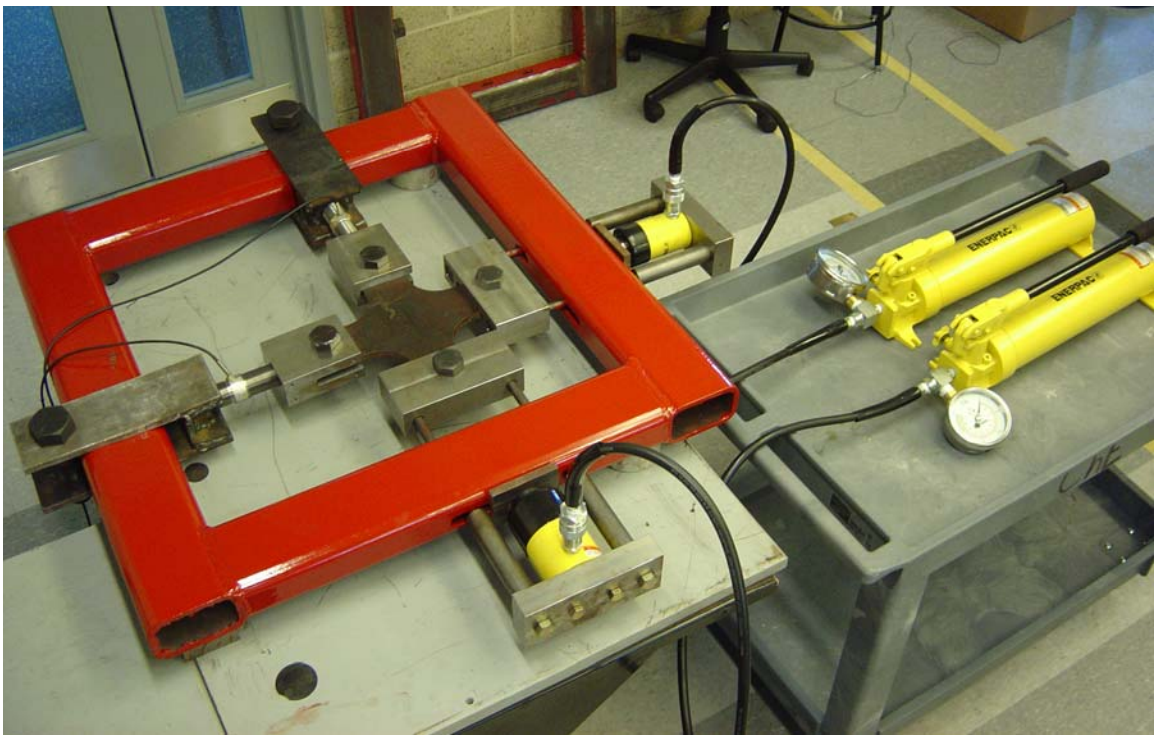

Figure 4: Assembled AE test platform.

Task 3.0 – Design and Development Data Fusion Algorithms

This report describes a suite of sensor data fusion algorithms developed for characterizing the pipe-wall condition of gas transmission pipelines when inspected using more than one method of non-destructive testing. The system that is designed aims to synergistically combine information that is present not only in heterogeneous sensors (for example, magnetic, ultrasonic and thermal) but also in heterogeneous data-sets (for example, “hits” obtained during acoustic emission inspection and images obtained from magnetic flux leakage testing). The objective of the data fusion algorithms is to improve the accuracy and reliability of pipeline monitoring by providing the location, size and shape of pipe-wall anomalies.

Subtask 3.1 – Development of measures for complementarity and redundancy of information in fused signals

A mathematical model of human monoscopic vs. stereoscopic vision (see Figure 5) can be employed for developing a data fusion algorithm. Consider an instance where there are two similar objects in one's field of view. One object is smaller and relatively closer to the observer while the second object is situated farther from the observer, and is larger than the first object. If one were to view this scene with only one eye, the image perceived on the retina would be that of two objects of identical size. Viewing the scene with both eyes, a separate and unique image is developed in each eye – with two separate, dissimilar images of the same scene, the brain can then fuse the images to develop fairly accurate estimates of the size and distance of the objects.

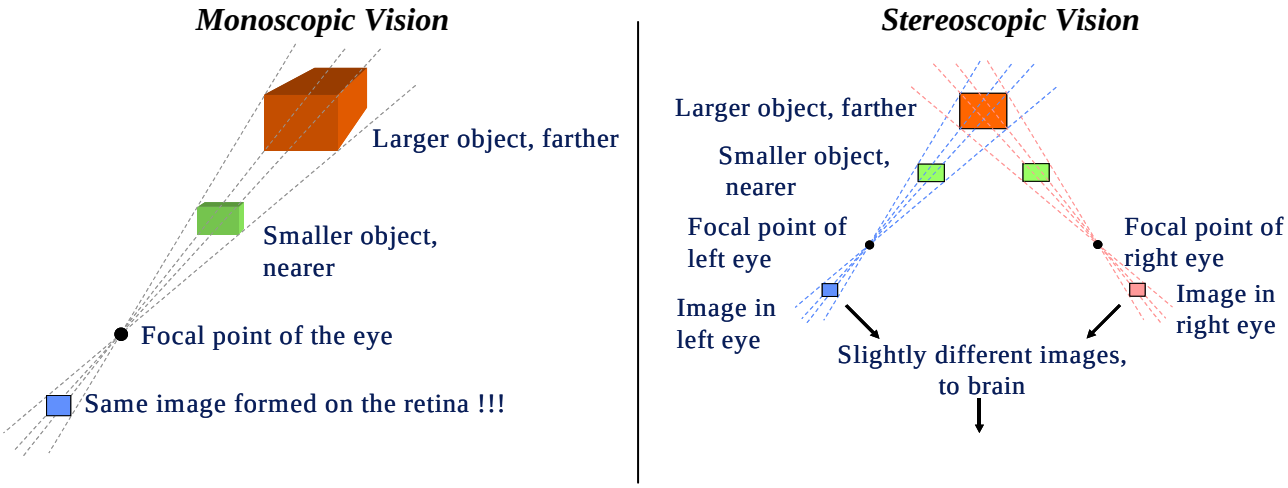

Figure 5: Model of human vision system - monoscopic vs. stereoscopic vision.

This stereoscopic vision process can be modeling mathematically with the following equation [1]:

$$g\left(x_1(d,l), x_2(d,l)\right) = h(d) \tag{1}$$

where x_1 and x_2 represents the images seen by each eye, which are dependent on object distance, d, and object size, l. The resulting perception of distances of each of the objects is provided by the function, $h(d)$. The function g, fuses the information present in each of the original images, x_1 and x_2 and can be modeled as a universal approximator given by the radial basis function neural network [2]

$$g = \sum_{j=1}^{m} \lambda_j \phi(\| x_i - c_{ij} \|) \tag{2}$$

where λ denotes the weights of the hidden layer nodes in the network and ϕ is a Gaussian basis given by

$$\phi_{ij}(\| x_i - c_{ij} \|) = e^{-\frac{|xi - c_{ij}|^2}{2\sigma^2}} \tag{3}$$

where c_{ij} is the basis center (mean) and σ is the radius (variance) of the Gaussian kernel.

This stereovision model can be employed for multi-sensor data fusion, as follows. When NDE images that are obtained from different inspection methods are fused, the fused image can be assumed to contain two main types of information that are related to the characteristics of the test object: redundant and complementary information. Redundant information is the information related to the defect that is common among different inspection methods and can be used to increase the reliability of the defect characterization result. Complementary information is the defect related information that is unique to each inspection method and can be used to improve the accuracy of defect characterization. Figure 6 pictorially depicts the redundant and complementary information in the data fusion process.

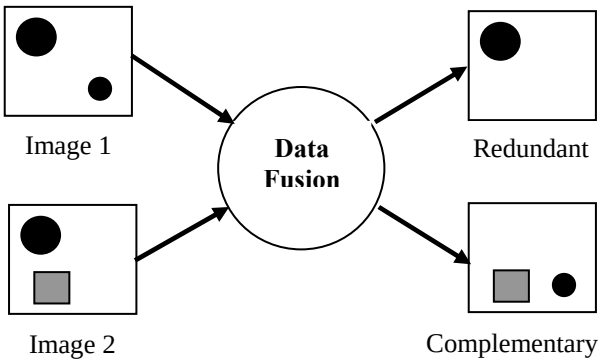

Figure 6: Illustration of redundant and complementary information in multi-sensor data fusion.

The stereovision model is now applied as follows. Let $x_1(r_1, c_1)$ and $x_2(r_1, c_2)$ be two different NDE images that are the results of the inspection of the same object using two different inspection modalities. The variable r represents the redundant information features and is the same for both images. Likewise, the variables c_1 and c_2 represent the complementary

information features for each image. A function that extracts the redundant defect related information, $h_1(r)$, between $x_1(r_1, c_1)$ and $x_2(r_1, c_2)$ can be defined as:

$$f\{x_1(r,c_1), x_2(r,c_2)\} = h_1(r) \tag{4}$$

and the function that extracts the complementary information can be defined as

$$f\{x_1(r,c_1), x_2(r,c_2)\} = h_2(c_1,c_2) \tag{5}$$

Both these functions are RBF neural networks, described in Equation (2).

Subtask 3.2 – Development of algorithms for defect identification

Learn++ is a novel algorithm capable of incremental learning of additional data, estimating classification confidence and combining information from different sources [3]. Learn++ employs an ensemble of classifiers approach for this purpose. Figure 7 conceptually illustrates the underlying idea for the Learn++ algorithm. The white curve represents a simple hypothetical decision boundary to be learned. The classifier's job is to identify whether a given point is inside the boundary. Decision boundaries (hypotheses) generated by base classifiers (BC_i, $i=1,2,\ldots 8$), are illustrated with simple geometric figures. Hypotheses decide whether a data point is within their decision boundary. They are *hierarchically* combined through weighted majority voting to form composite hypotheses H_t, $t=1,\ldots 7$, which are then combined to form the final hypothesis H_{final}. In this study, different ensemble classifiers, each trained with signals of different modalities used as features, were incorporated into the NDE signal identification system. To work in data fusion mode, Learn++ was modified according to structure in Figure 8, combining the pertinent information from all identifiers.

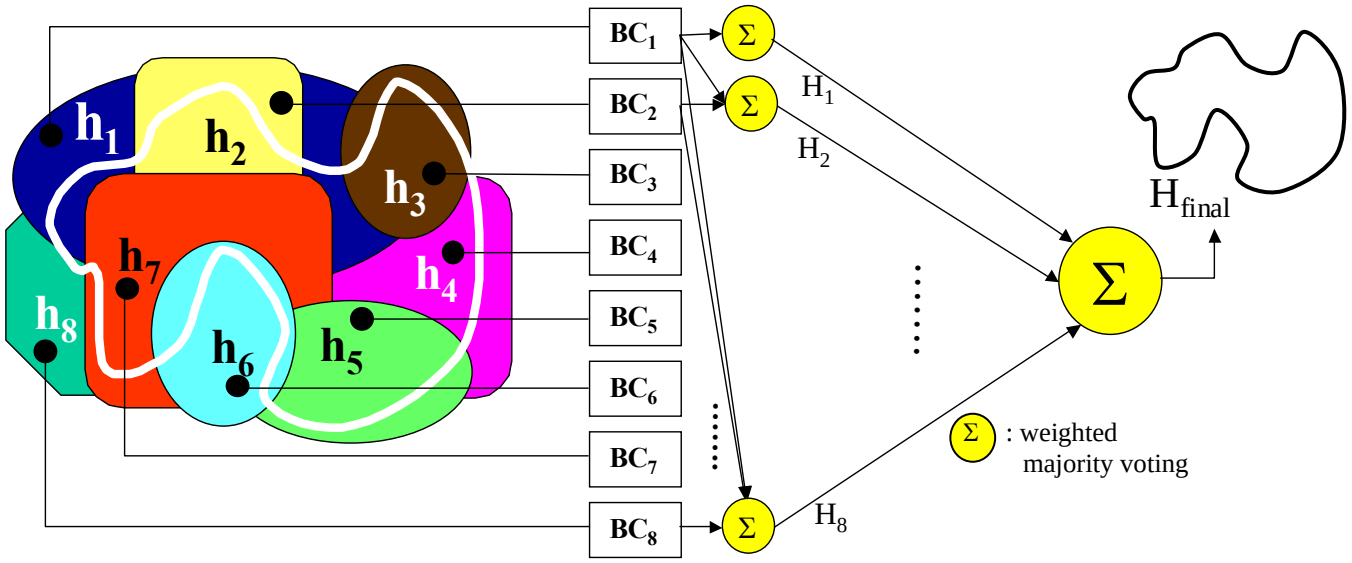

Figure 7: Conceptual illustration of the Learn++ algorithm.

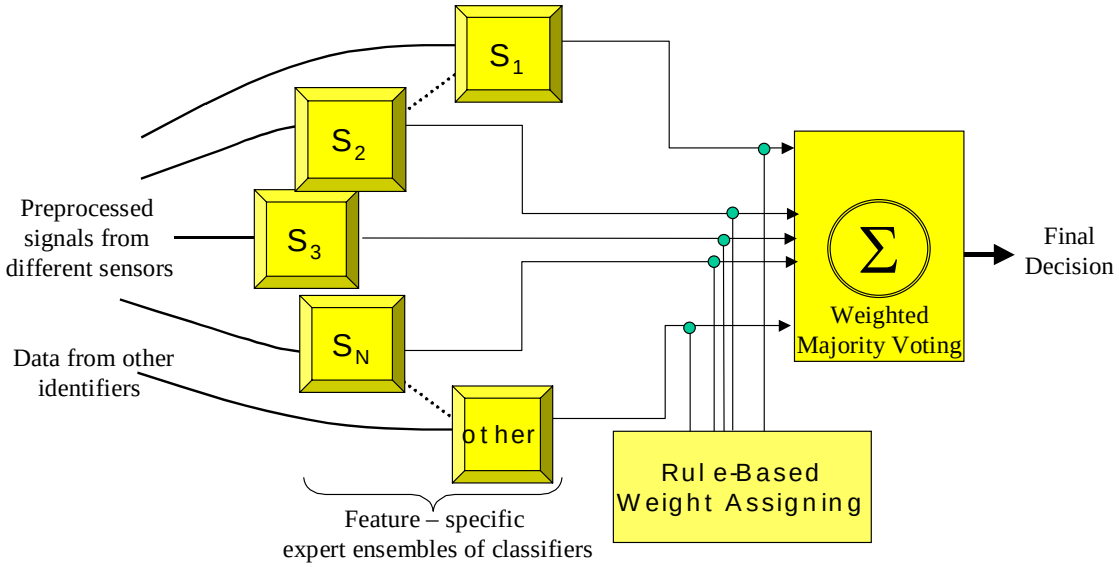

Figure 8: Learn++ for data fusion.

Subtask 3.3 – Development of algorithms for defect sizing

In order to train the artificial neural network for defect characterization, it is necessary to indicate the desired complementary and redundant information between the two NDE inspection methods. In this report, since the actual defect size, shape, depth and location is known for the specimen suite, these definitions can be made by comparing the NDE signature for each of the inspection methods with the size, shape, depth and location of the defect. Figure 9 illustrates this

definition process. Complementary information in two NDE images are defined as those distinct pixels in each of the NDE signatures that are present in the defect region, but are not shared between them. Redundant information in two NDE images are defined as those common pixels that are present in both NDE signatures and are also present in the defect region.

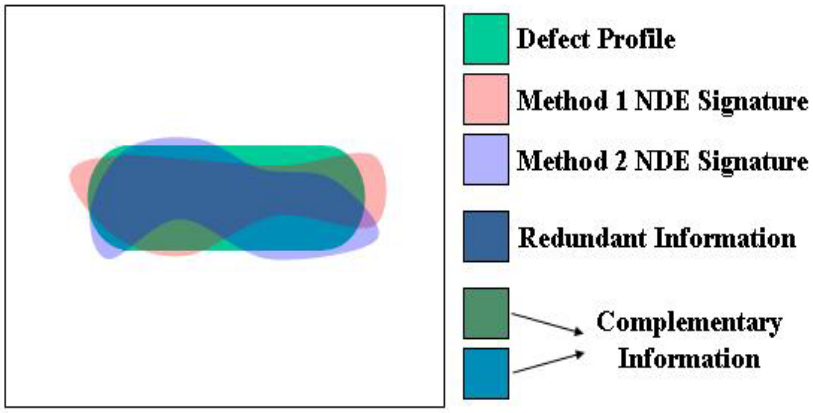

Figure 9: NDE image signatures used to define redundant and complementary information.

In order to perform a redundant and complementary data extraction process on acoustic emission data it is first necessary to define how the location of AE source points corresponds to the position and shape of the actual defect. Unlike the homogeneous NDE sources, acoustic emission data does not provide the user with geometrical shape information of the defect, but only provides an estimation of where the defect is located. To perform redundant and complementary data extraction it is first necessary to relate the acoustic emission point data to a specific defect location area. Once this process has been performed the homogeneous data fusion process can be employed to extract the redundant and complementary information.

The acoustic emission testing performed in the laboratory seemed to indicate that the acoustic emission source locations do not fall directly over the defect area, but rather form clusters located around the defect. From this information the assumption can be made that the defect is located somewhere in the area surrounded by the AE source locations. In order to perform the data fusion process it is necessary to characterize this area of the defect so it can be combined with the other NDE testing modalities. The first method in characterizing this area was to perform a K-means clustering algorithm on the raw AE data to determine how many clusters the data had been formed into and which points fell into each cluster. Figure 10 shows the AE data from the uniaxial specimen with the 0.16 inch deep defect after the cluster algorithm has been performed. In this case two separate classes of data have been clearly defined on either side of the defect.

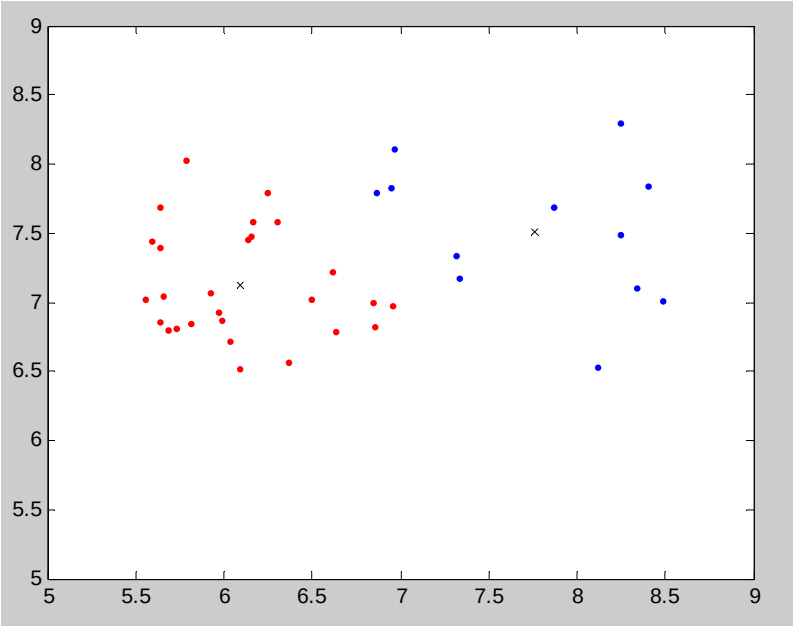

Figure 10: K-means clustering on AE data of uniaxial specimen with 0.16" deep defect.

After the two classes of data have been defined, a Parzen windows density estimation [4] is performed on each class separately which can be seen in Figure 11. The Parzen windows approximation fits a two-dimensional Gaussian plot over each class of the data to demonstrate the areas of higher density of the AE sources.

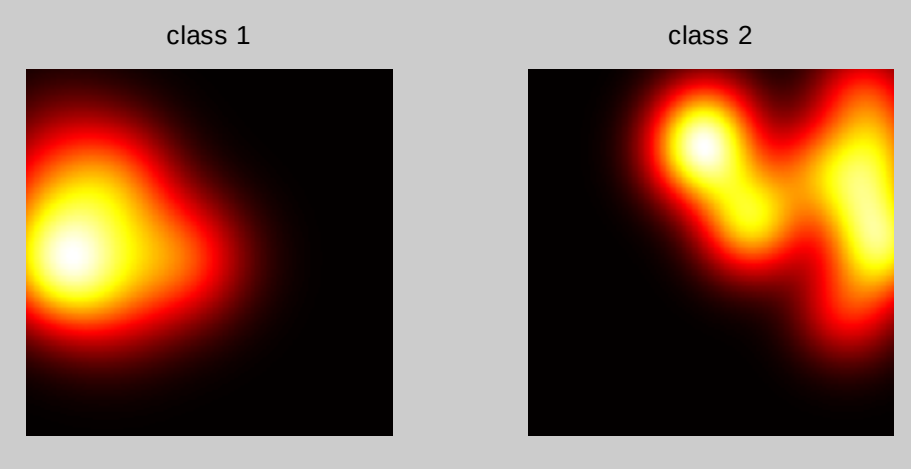

Figure 11: Parzen windows density estimation of each class separately.

The Parzen window images are then overlaid on top of each other. Where the density estimations overlap becomes the region in which the AE data predicts the presence of a defect. To perform this process the Parzen window images are converted to binary images seen in Figure 12. A logical AND is then performed between the two image matrices to determine where the images overlap.

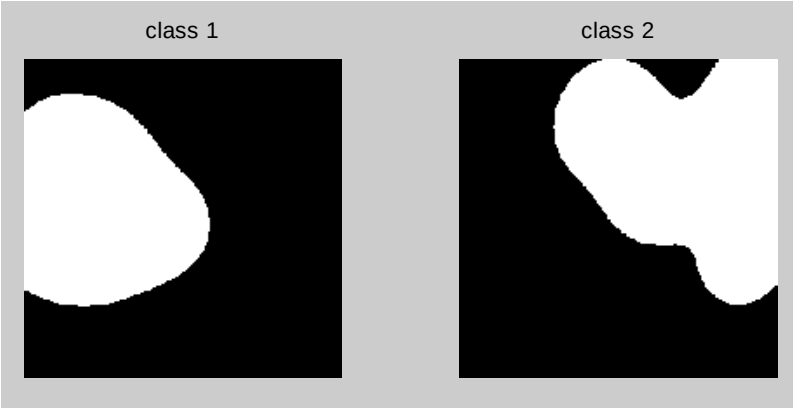

Figure 12: Binary representation of Parzen windows AE images.

For the AE tests performed in this project, the number of clusters of data surrounding the defect could vary from one to four classes. The overlapping areas of the Parzen windows images were then weighted from 0 to 1 in increments of 0.25, i.e., if two classes overlap, the overlapped area will be weighted at 50 percent, and for three classes overlapping 75 percent and so on. This allows for a high volume of data surrounding the defect to have a stronger influence on the data fusion process. Figure 13 shows the resulting defect area represented from the acoustic emission source data shown above in Figure 10.

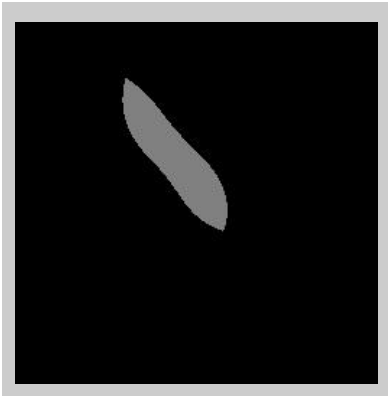

Figure 13: Defect location representation from AE data.

The above process was performed on all of the acoustic emission data to generate AE location estimation plots. The resulting images seen in Figure 14 can then be input to the redundant and complementary data extraction algorithm.

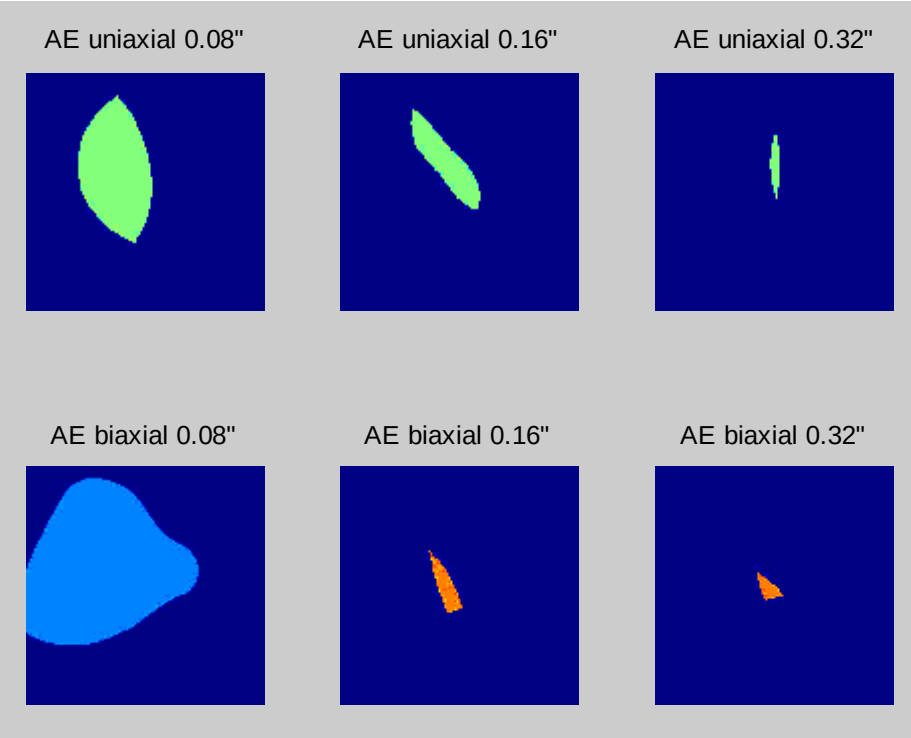

Figure 14: AE location estimation plots for the data fusion algorithm.

Task 5.0 – Recommendations for Effective Data Management

This report describes the use of virtual reality (VR) platforms for effectively managing the voluminous amounts of inspection data that is generated when pipeline sections are interrogated using multiple sensor methods. Virtual reality has emerged as a powerful visualization tool for design, simulation, and analysis in modern complex industrial systems. Virtual reality can be defined as any system that allows a user to have immersion, navigation, and interaction. A fully immersive environment is one in which the user is completely engulfed in the virtual world and sensory input for the real world is completely blocked. Navigation in the virtual world allows the user to move to different regions within the world. Finally, interaction is the user's ability to interact with the data. Interaction allows the user to not only see the data, but manipulate it as well [5]. All of these factors contribute to the main thrust of the virtual environment, presence. Presence in a virtual world is the feeling of an accurate depiction of reality in the virtual environment [6].

The creation of presence in a virtual world serves two main purposes. First, it allows the user to visualize data in true three-dimensional representations. Also, it allows the user to visualize phenomena and data such that additional insight is gained. With full control over the virtual world, the designer can create a world such that the user can gain a perspective that would otherwise be difficult if not impossible to obtain [7]. The creation of the virtual world focuses on component representation and component registration. Components with higher detail will create a greater sense of presence. The tradeoff, however, is that increased detail places more demands on the hardware. If the hardware becomes bogged down the world can lag; the sense of presence will then be lost [8]. Components and data therefore need to be represented with minimum resolution needed for the specific purpose.

VR is a well-suited platform in which the framework can be intended to support not only the integration of data for visual, interactive, and immersive displays, but also provide a method for performing risk analysis. Inside the virtual world, the user could be given the ability to evolve the data over time and create various scenarios. An evolutionary virtual world allows the user to ask "What if…?" The virtual world will then evolve over time as a function of the user inquiry and system data. Using the evolutionary scenario that has unfolded, the user is empowered to more thoroughly analyze the data and draw relevant conclusions. The data integration via VR paradigm is illustrated in Figure 15. Multi-sensor pipeline inspection data is obtained from the following testing methods – magnetic flux leakage (MFL), ultrasonic testing (UT), thermal

imaging, and acoustic emission (AE) testing. This data is input into artificial neural nets to classify data signatures, and predict anomaly geometries. CAD models of the pipeline are used for registration of the data. The final component of the virtual world is information obtained from the geographic information system (GIS). The GIS information is used to assess environmental concerns and provide information about the specific location of the pipeline.

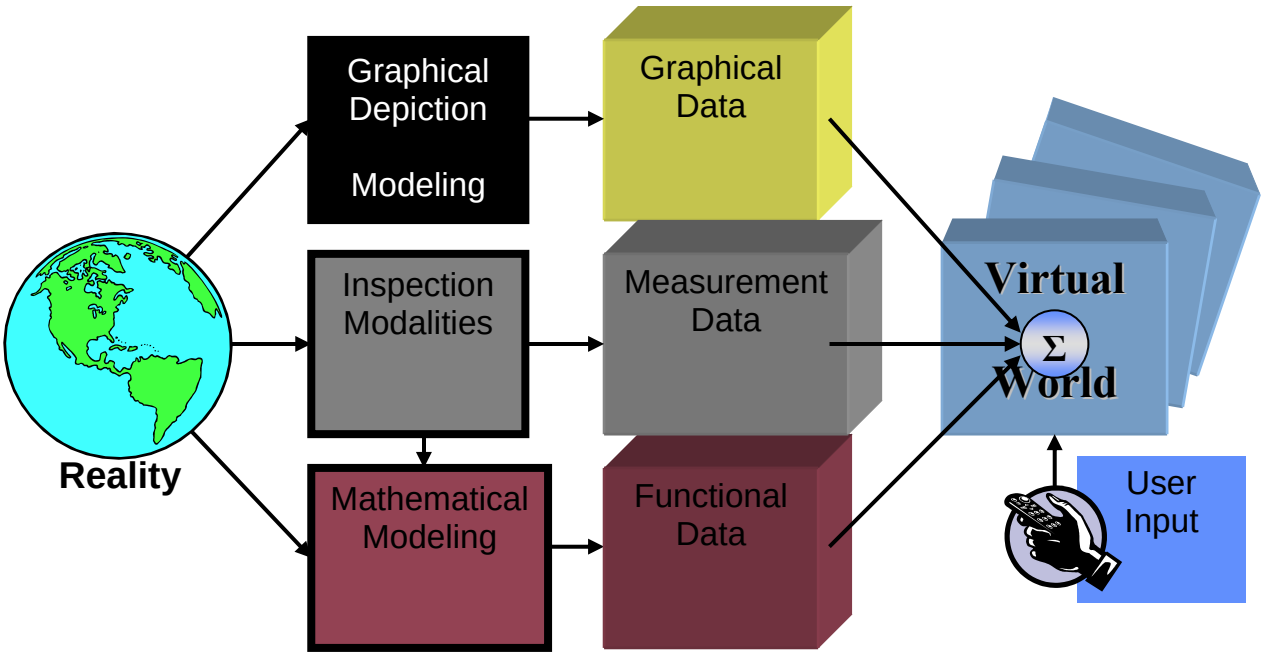

Figure 15: An overview of the data integration process for the NDE of gas transmission pipelines.

There are numerous ways data in a virtual world can be described. The most common methods for categorizing data are dividing it according to its representation in the virtual world or its purpose in the virtual world [9]. For most data integration applications the information can be broken down into three categories - graphical, functional, and measurement. Each category can then have several different representations according to the specific software used and desired results.

Graphical objects are traditionally the basis of a virtual world. The graphical objects in the virtual environment represent objects that exist in the actual environment. In inspection applications the representations would include the object being analyzed and any additional objects that are present in the environment. Graphical objects can be modeled using dimensioned drawings, or created visually using a picture or reference object. Graphical objects must be created with detail suitable to fulfill their role for a specific application.

Measurement data is the raw data obtained from any type of sensor. Multi-sensor data integration focuses on representing each data modality individually and in tandem with the other modalities. Depending on the type of data that is obtained, the measurement data can take on a variety of representations. Each data point collected can be represented using a point representation or glyphs. Interpolation between points can be represented through the use of a color slice. A topological representation can be used to vary the data representation spatially as a function of the value. Three-dimensional surfaces can also be created to represent the true form of the data collected.

For each sensor and each modality of data there may not be only one representation that best fits the data. Each application will have specific visualization needs, and the data representations should be tailored to those needs. Multiple representations of a single type of data are also helpful for a user analyzing complex data sets.

Functional components are representations of processed or calculated data. Analyzing raw data is not usually sufficient in most inspection applications. Neural nets or other algorithms can be used to help classify certain areas within the data sets. Components (the graphical objects) can be identified or flagged such that only the areas of interest are analyzed. Evolutionary algorithms can be designed to predict how the current state of the world might evolve over time for a given set of parameters. Analysis using first principles or finite element analysis can also be used to see how measured data compares to theoretical data. Like the measured data, each type of functional data representation will have a representation consistent with the purpose of that data.

Graphical Data

Graphical data represents the objects being investigated and the environment in which those objects exist. For this application there are two types of graphical objects being integrated, pipeline components and GIS information. The component models represent the object being investigated and the GIS data conveys information about the environment of the pipeline

There are a number of base graphical objects to represent a pipeline. These include a section of pipe, flange, weld, sleeve, t-section, check valve, ball valve, anchor, and anomalies (crack, pit, etc.). Each component can be modeled using a CAD program. The library of modeled components can then be assembled to create the pipeline that is being inspected. Drawings of the pipeline system can be used to manual piece together the various library components to make an increasingly complex network of pipes. Automated assembly algorithms can also be

constructed to allow construction of the pipeline network in the virtual world. The library can also have multiple detail levels for each component. Using lower detail allows for the creation of expansive pipeline networks. When an area of interest is identified, a subsection of the network can be subsequently generated using the components with finer details.

The geographic information system can give a great deal of information about the location of the pipeline network. The GIS can give information about the topography, land usage, location of rivers, roads, buildings, etc. This information can be integrated into the virtual environment such that the user can gain insight into the location details of the pipeline. Under certain conditions remediation measures are determined based on the location of the pipe in question. Integrating GIS information into the virtual environment allows the user to have not only physical location, but additional sociologic information.

Functional Data

Functional data can be obtained through any type of mathematical model. For this application the functional data is a function of the measured data. Using the data gathered, artificial neural nets can be used to classify the data signatures. The category labels for the output of the neural net are the library components for the graphical library. ANN predictions can be used in two different ways. The predictions can be used to assist in visually classifying the signatures and searching for anomalies within the data collected; also, the predictions can be used to construct a pipeline network. For each neural net prediction the corresponding component piece can be obtained from the graphic library and appended onto the network. This predicted network can be easily compared to the actual network.

If an anomaly is present ANNs can be used to further classify the depth and geometry of the anomaly. Using multiple modalities of data, predictions can be made on the size and shape of an anomaly. This information can be represented in the virtual world, and used to help assess the pipeline integrity.

Measurement Data

Measurement data has been collected using a variety of NDE methods including magnetic flux leakage (MFL), ultrasonic testing (UT), thermal imaging, acoustic emission (AE), and thermal imaging.

Results

Task 4.0 – Design and Development of the Validation Test Platform

Subtask 4.2 – Test Platform Development

The test platform was subjected to a finite-element methods (FEM) analysis using COSMOS Works in order to simulate loading conditions. FEM analysis was performed on the new clamping brackets to ensure they could handle the maximum load of 30 ksi. Figures 16 and 17 contain FEM analysis diagrams of both bracket types. Figure 16 shows that the loading clamping bracket experienced a maximum force of 27,900 psi, which is well under the maximum yield stress of the steel. Figure 17 shows the rear of the load-cell clamping block where the load cell will be threading into the back of the block. This block experienced a maximum force of 33,590 psi, which also is under the yield stress of the steel.

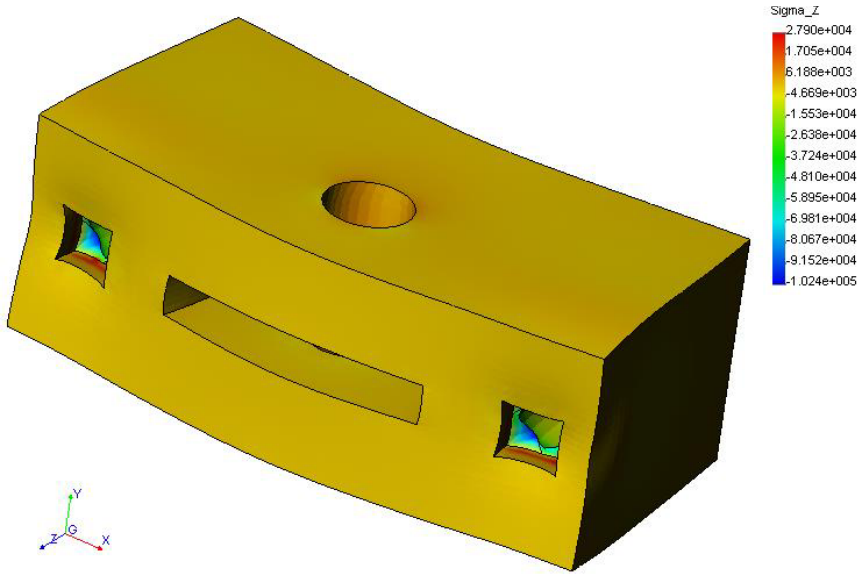

Figure 16: FEM analysis of the design of the loading clamping block.

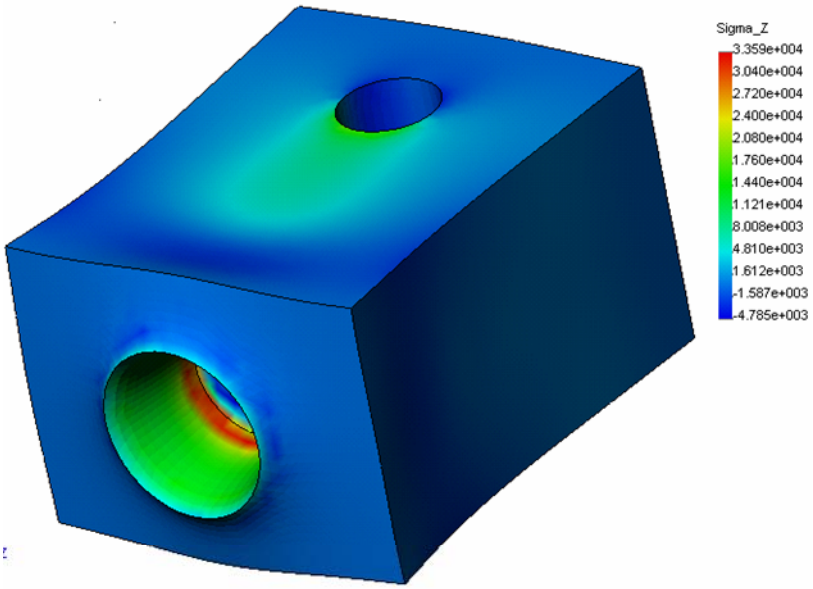

Figure 17: FEM analysis of the design of the load cell clamping block.

FEM analysis on the hydraulic assembly was performed using COSMOS Works and can be viewed in Figure 18. The analysis demonstrates that the hydraulic assembly will experience a maximum of 23,850 psi, which is well under the yield stress of the Grade 8 bolts (120,000 psi), C-1018 steel rods (50,000 psi), and the A-572 grade 50 steel (58,000 psi).

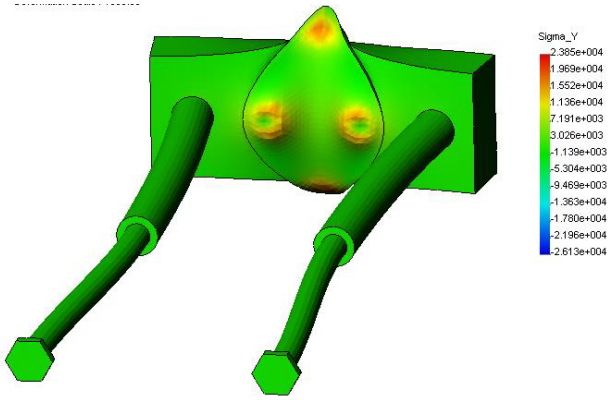

Figure 18: FEM analysis of the design of the hydraulic assembly.

Subtask 4.3 – Obtain Multi-Sensor NDE Data.

Magnetic flux leakage (MFL) testing was performed on the specimen suite outlined in the previous section. The specimens tested were those containing simulated pitting defects with a rectangular slotted shape machined from the specimen. Each of the specimens was then energized with 200 amps to induce the needed magnetic field. A Hall probe was then used to

record any magnetic leakage around the defect. Figure 19 contains the resulting magnetic images. Rows 1 through 4 show the progression of increasing defect depth starting with no defect followed by 0.1", 0.2", and 0.3" deep. Column A, B, and C display the varying specimen thickness with Column A being ½" thick, B 3/8" thick, and C 5/16" thick. Table 2 has been included to further specify the specimens and defects.

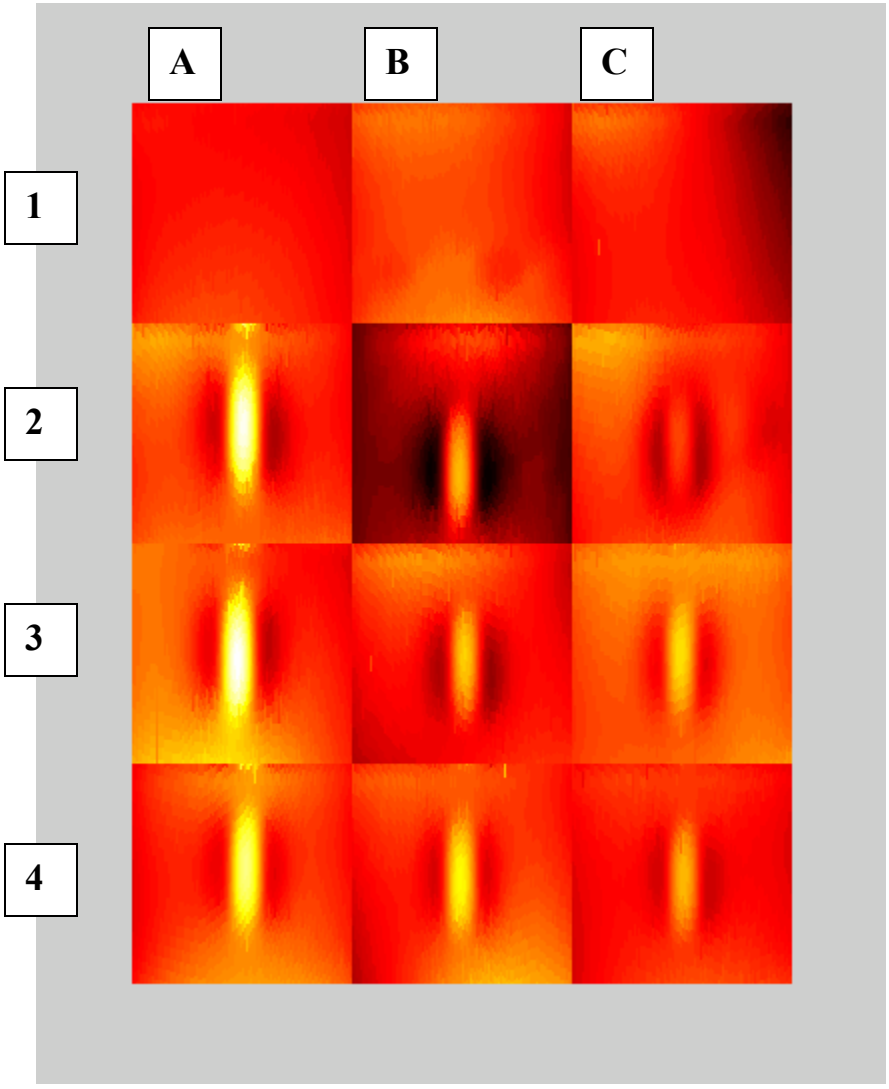

Figure 19: MFL scans of slotted shape defects.

Table 2: Slotted shape defects scanned using MFL and UT.

Specimen #	Plate thickness (in)	Defect Type	Defect Depth (in)
A1	0.5	None	N/A
A2	0.5	Pitting	0.3005
A3	0.5	Pitting	0.198
A4	0.5	Pitting	0.0945
B1	0.375	None	N/A
B2	0.375	Pitting	0.298
B3	0.375	Pitting	0.199
B4	0.375	Pitting	0.1105
C1	0.3125	None	N/A
C2	0.3125	Pitting	0.303
C3	0.3125	Pitting	0.1955
C4	0.3125	Pitting	0.0995

Ultrasonic testing (UT) was also performed on the same test specimens. Each specimen was submerged in water and scanned with a 10MHz UT transducer. The threshold and gating of the UT signal was adjusted to display changing depths of the specimen defects. Figure 20 contains the resulting time-of-flight (tof) ultrasound images. Rows 1 through 4 show the progression of increasing defect depth starting with no defect followed by 0.1", 0.2", and 0.3" deep. Column A, B, and C display the varying specimen thickness with Column A being ½" thick, B 3/8" thick, and C 5/16" thick. Table 2 has been included to further specify the specimens and defects.

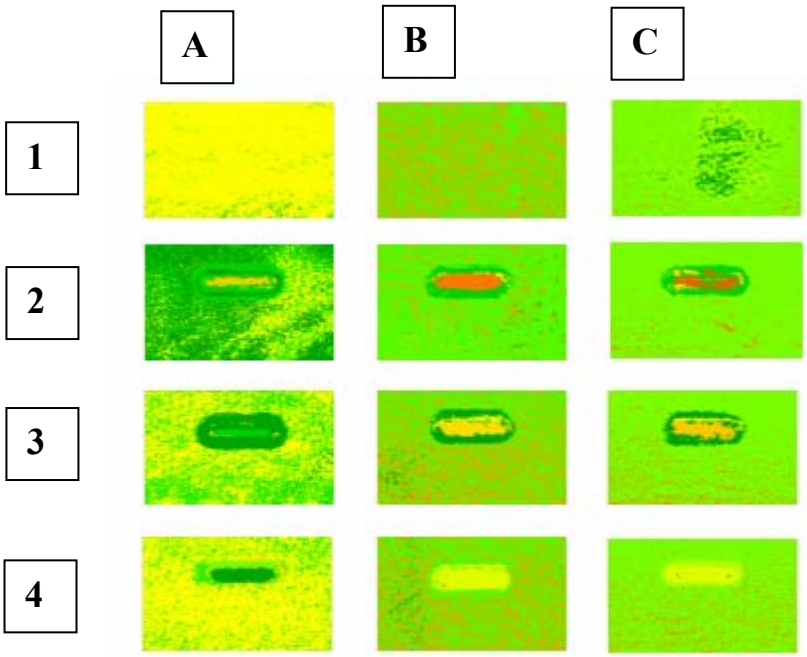

Figure 20: UT scans of slotted shape defects.

Thermal imaging NDE was performed on the specimen suite. The specimens tested were those containing simulated pitting defects with a rectangular slotted shape machined from the specimen; the specimen suite is described in Table 1. The thermal imaging test set-up consists of a high-power 110 W Halogen lamp that is sinusoidally excited at a rate of 8-10 seconds/cycle. The specimen is placed on an optical table and is thermally insulated with an Aluminum honeycomb panel. The thermal images of the test specimens are captured using a FLIR Systems Microbolometer camera. The images were obtained at 1 second intervals over the excitation cycle. Five images at equally spaced time intervals over each cycle were processed to extract the phase images – these are shown in Figure 21. The images are scaled and registered to reflect a resolution of 100 pixels/inch. It can be noticed that the defect related information in the thermal phase images is less than that contained in the UT and MFL NDE images.

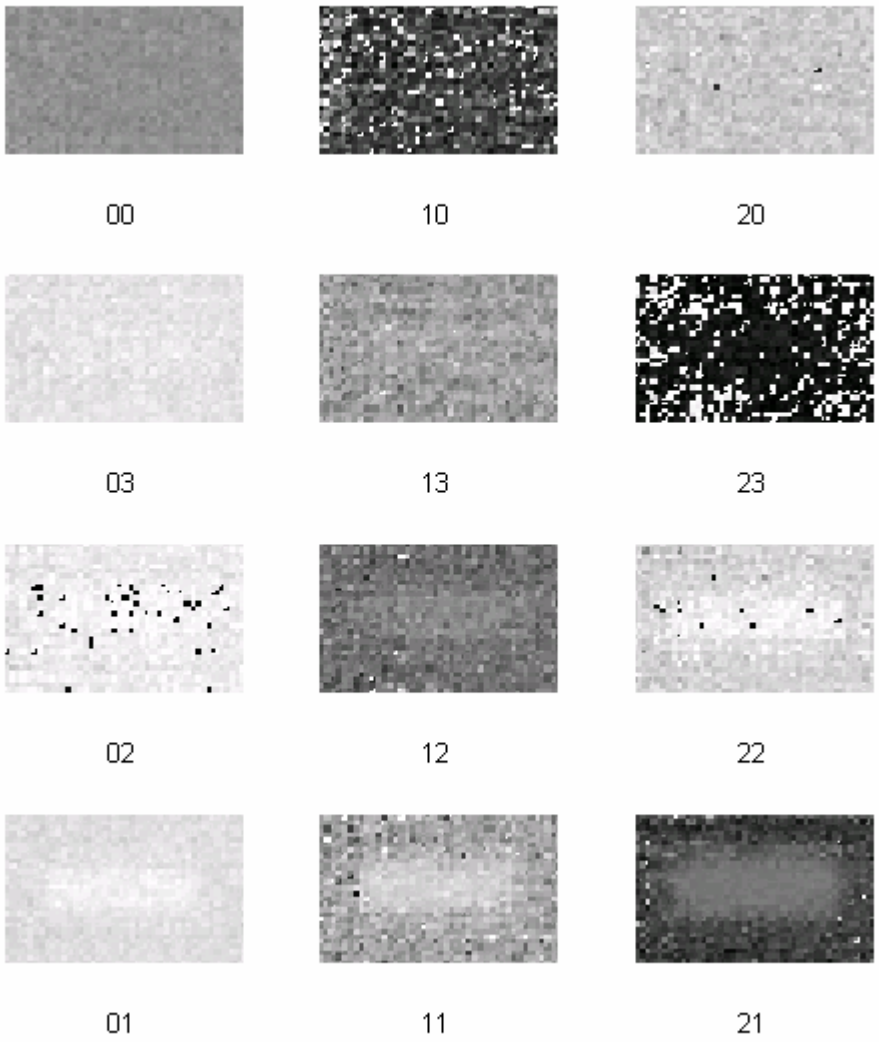

Figure 21: Thermal phase images of slotted defects in the test specimen suite shown in Table 1.

Task 3.0 – Design and Development Data Fusion Algorithms

Subtask 3.2 – Development of algorithms for defect identification

The Learn++ algorithm's data fusion capabilities were evaluated on the MFL and UT data obtained from the specimen suite described in a previous report. We were particularly interested in whether we could improve the generalization performance of the algorithm (the correct classification performance on the validation data not seen by the algorithm during training) when data from two different NDE modalities (namely, MFL and UT) are fused. To test this performance, we have partitioned the test-specimen suite into two sections, ten to be used for

training the algorithm, and eleven to be used for validation. We had a total of 5 categories, namely pitting, crack, mechanical damage, weld and no defect. Our goal was to compare the classification performances when trained with only MFL or UT data to the performance when the data was combined through the Learn++ algorithm. We have used the multilayer perceptron (MLP) neural network as the base classifier with Learn++ and we have tested the algorithm with several MLP architectures from 10 hidden layer nodes to 50 hidden layer nodes and varying error goals [10].

Tables 3 and 4 summarize signal classification (percentage of correct classification of NDE signature) using MFL and UT signatures separately, without data fusion. The classification results after data fusion using the Learn++ algorithm is indicated in Figure 22.

Table 3: Signal classification results using MFL signatures only.

MFL analysis										
		Number of Hidden Layer Nodes								
		10	***15***	***20***	***25***	***30***	***35***	***40***	***45***	***50***
Error Goal	***0.01***	80.00	86.70	86.70	73.30	86.70	80.00	80.00	86.70	86.70
	0.02	93.30	86.70	86.70	80.00	80.00	93.30	80.00	80.00	80.00
	0.03	73.30	80.00	73.30	86.70	86.70	86.70	80.00	73.30	80.00
	0.04	86.70	73.30	80.00	93.30	80.00	73.30	80.00	86.70	86.70
	0.05	80.00	66.70	73.30	80.00	73.30	93.30	86.70	66.70	80.00
	0.06	73.30	80.00	93.30	86.70	73.30	66.70	86.70	66.70	80.00
	0.07	73.30	73.30	73.30	80.00	80.00	73.30	66.70	66.70	73.30
	0.08	86.70	73.30	80.00	73.30	60.00	93.30	73.30	73.30	60.00
	0.09	80.00	60.00	66.70	80.00	80.00	80.00	73.30	73.30	80.00
	0.1	66.70	80.00	86.70	73.30	73.30	73.30	60.00	80.00	73.30
		Hidden Layer Mean								
		79.33	76.00	80.00	80.66	77.33	81.32	76.67	75.34	78.00
		Hidden Layer Standard Deviation								
		7.984297	8.441564	8.320791	6.641486	7.839792	9.830203	8.469297	7.73135	7.74281
					Global Mean					
						78.29				

Table 4: Signal classification results using UT signatures only.

UT analysis										
	Number of Hidden Layer Nodes									
Error Goal	***10***	***15***	***20***	***25***	***30***	***35***	***40***	***45***	***50***	
0.01	73.33	86.67	73.33	80	100	86.67	86.67	80	93.33	
0.02	86.67	86.67	86.67	86.67	73.33	86.67	93.33	66.67	73.33	
0.03	86.67	93.33	80	86.67	80	86.67	86.67	86.67	86.67	
0.04	86.67	93.33	86.67	66.67	86.67	86.67	93.33	86.67	80	
0.05	86.67	100	86.67	86.67	86.67	86.67	86.67	86.67	93.33	
0.06	73.33	73.33	80	86.67	80	86.67	86.67	93.33	86.67	
0.07	66.67	86.67	86.67	86.67	80	86.67	66.67	86.67	86.67	
0.08	66.67	86.67	93.33	86.67	86.67	86.67	80	73.33	86.67	
0.09	73.33	73.33	66.67	86.67	80	80	80	93.33	80	
0.1	66.67	86.67	80	80	73.33	80	66.67	86.67	80	
	Hidden Layer Mean									
	76.67	86.67	82	83.33	82.67	85.33	82.67	84	84.67	
	Hidden Layer Standard Deviation									
	9.03	8.31	7.73	6.48	7.83	2.81	9.53	8.43	6.32	
				Global Mean						
					83.11					

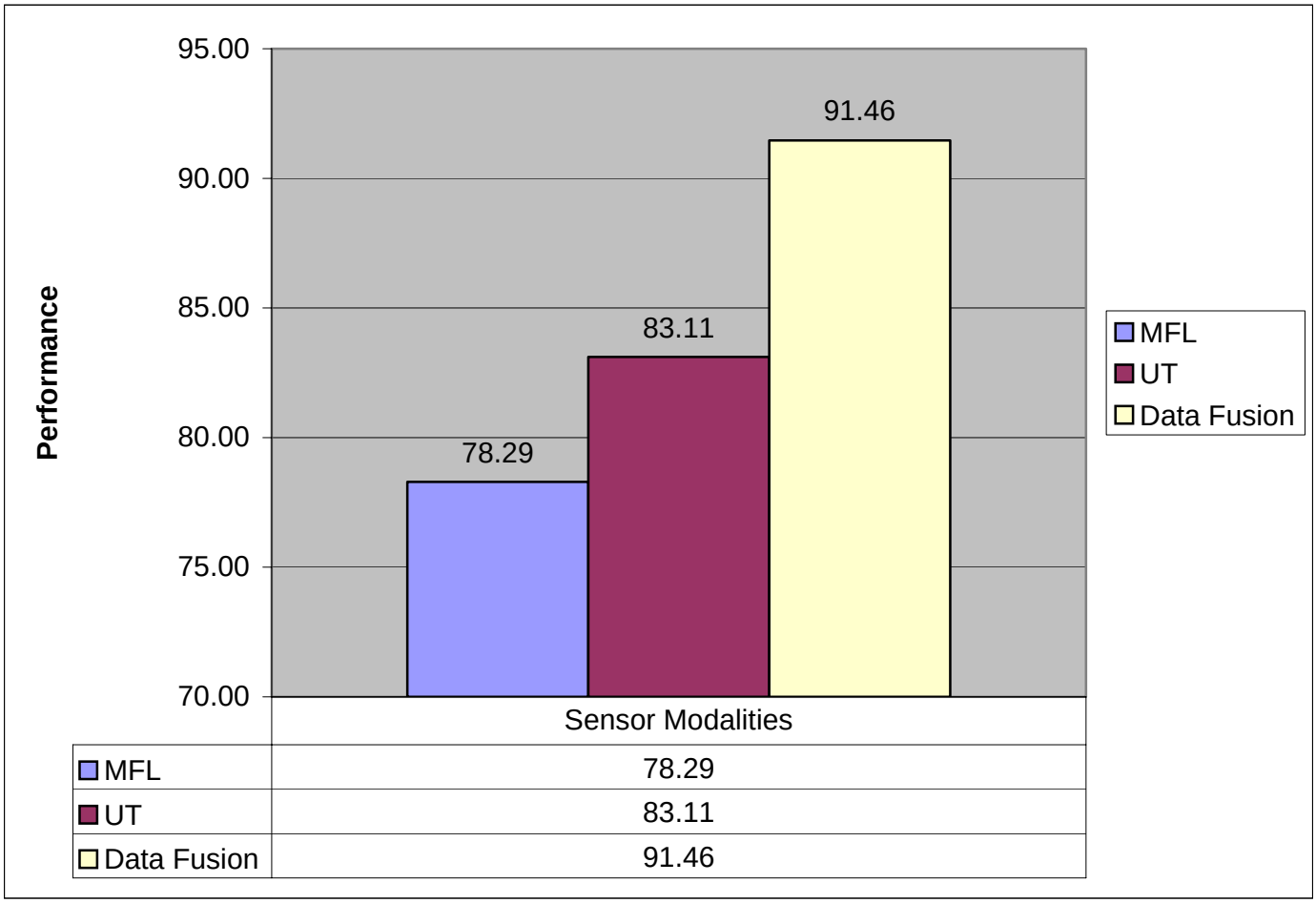

Figure 22: MFL and UT data fusion results for signal identification using Learn++.

Subtask 3.3 – Development of algorithms for defect sizing

Homogeneous Training and Test Datasets

The homogeneous data fusion is performed on the NDE inspection data collected from the ultrasound, MFL, and thermal imaging systems. In each test platform the twelve specimens have been scanned twice on two separate instances to provide additional data for training and testing the neural network. The data fusion technique is performed on three different instances between: UT & MFL, Thermal & UT, and MFL & Thermal. Each test sequence includes three separate trials that vary the training and test data inputted into the network. The training and test data segmentation for each trial is listed below in Tables 6 through 8.

Table 6: Trial 1 training and test dataset.

Specimen #	Plate thickness (in)	Indication	Defect Depth (in)
00a	0.5	None	N/A
03a	0.5	Pitting	0.0945
02a	0.5	Pitting	0.198
01a	0.5	Pitting	0.3005
10a	0.375	None	N/A
13a	0.375	Pitting	0.1105
12a	0.375	Pitting	0.199
11a	0.375	Pitting	0.298
20a	0.3125	None	N/A
23a	0.3125	Pitting	0.0995
22a	0.3125	Pitting	0.1955
21a	0.3125	Pitting	0.303
00b	0.5	None	N/A
03b	0.5	Pitting	0.0945
02b	0.5	Pitting	0.198
01b	0.5	Pitting	0.3005
10b	0.375	None	N/A
13b	0.375	Pitting	0.1105
12b	0.375	Pitting	0.199
11b	0.375	Pitting	0.298
20b	0.3125	None	N/A
23b	0.3125	Pitting	0.0995
22b	0.3125	Pitting	0.1955
21b	0.3125	Pitting	0.303

Training data Test data

Table 7: Trial 2 training and test dataset

Specimen #	Plate thickness (in)	Indication	Defect Depth (in)
00a	0.5	None	N/A
03a	0.5	Pitting	0.0945
02a	0.5	Pitting	0.198
01a	0.5	Pitting	0.3005
10a	0.375	None	N/A
13a	0.375	Pitting	0.1105
12a	0.375	Pitting	0.199
11a	0.375	Pitting	0.298
20a	0.3125	None	N/A
23a	0.3125	Pitting	0.0995
22a	0.3125	Pitting	0.1955
21a	0.3125	Pitting	0.303
00b	0.5	None	N/A
03b	0.5	Pitting	0.0945
02b	0.5	Pitting	0.198
01b	0.5	Pitting	0.3005
10b	0.375	None	N/A
13b	0.375	Pitting	0.1105
12b	0.375	Pitting	0.199
11b	0.375	Pitting	0.298
20b	0.3125	None	N/A
23b	0.3125	Pitting	0.0995
22b	0.3125	Pitting	0.1955
21b	0.3125	Pitting	0.303

 Training data  Test data

Table 8: Trial 3 training and test dataset

Specimen #	Plate thickness (in)	Indication	Defect Depth (in)
00a	0.5	None	N/A
03a	0.5	Pitting	0.0945
02a	0.5	Pitting	0.198
01a	0.5	Pitting	0.3005
10a	0.375	None	N/A
13a	0.375	Pitting	0.1105
12a	0.375	Pitting	0.199
11a	0.375	Pitting	0.298
20a	0.3125	None	N/A
23a	0.3125	Pitting	0.0995
22a	0.3125	Pitting	0.1955
21a	0.3125	Pitting	0.303
00b	0.5	None	N/A
03b	0.5	Pitting	0.0945
02b	0.5	Pitting	0.198
01b	0.5	Pitting	0.3005
10b	0.375	None	N/A

13b	0.375	Pitting	0.1105
12b	0.375	Pitting	0.199
11b	0.375	Pitting	0.298
20b	0.3125	None	N/A
23b	0.3125	Pitting	0.0995
22b	0.3125	Pitting	0.1955
21b	0.3125	Pitting	0.303

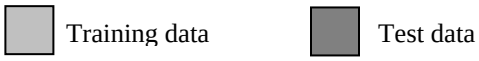

Typical results in Figures 23 (a) through (v) represent Trial 1 for MFL-UT combinations of NDE data, **with a red border surrounding the subplot figure of test data outputs. Included in each trial are the training data outputs and test data outputs of the neural network seen in the subplots (a) through (x). A red border surrounding the subplot figure designates the test data outputs**. The subplots (a) through (x) represent the output for the specimens listed in the order of the trial tables, with the specimens designated for testing shown last, with a red border. For example, subplot (a) represents the training input and output from Specimen 00a, while subplot (b) represents Specimen 03a, and so on. In certain combinations, outlying training data instances were excluded from training and testing, causing there to be fewer subplots in those cases. Each subplot figure is segmented into six images. The first row includes the input data from each of the NDE testing modalities. The second row represents the redundant and complementary output predicted by the algorithm while the third row shows the desired redundant and complementary output. All of the results are properly labeled and formatted in this manner.

There is an important difference to note between training data and test data. Training data is used to determine the synaptic weights of the network. Both training inputs and desired outputs must be provided to the network in the training process. In the case of training data seen in subplots in Figures 23 (a)-(v), the first row, labeled “inputs,” are the training inputs. The third row, labeled “desired output” are the outputs that the network is trained to produce when the associated inputs are given to the network. The second row shows the actual output that is produced when a fully trained network is given its own training data inputs as inputs. Test data, on the other hand, is never used to train the network. Therefore, the first row in a test data subplot is the actual input that is given to the network for testing. The second row is the actual (predicted) output of the network for test inputs; these are the test results. The images in the third row (created using the same technique that the training data desired outputs were created

with) show, for test data, what the network should be producing as output. These images in the third row provide a means of evaluating the predicted testing data outputs.

Keeping these key differences between training and testing data in mind, it is therefore desired for the redundant desired output image to closely resemble (in theory, be exactly like) the redundant output. Similarly, the complementary desired output image must resemble the complementary output, as closely as possible. This is true for all subplots, for both training and test instances. In training instances, close similarity illustrates that the synaptic weights of the network are optimal and in test instances, close similarity illustrates that the network is able to interpolate for new instances of input data.

Trial 1: UT & MFL Results

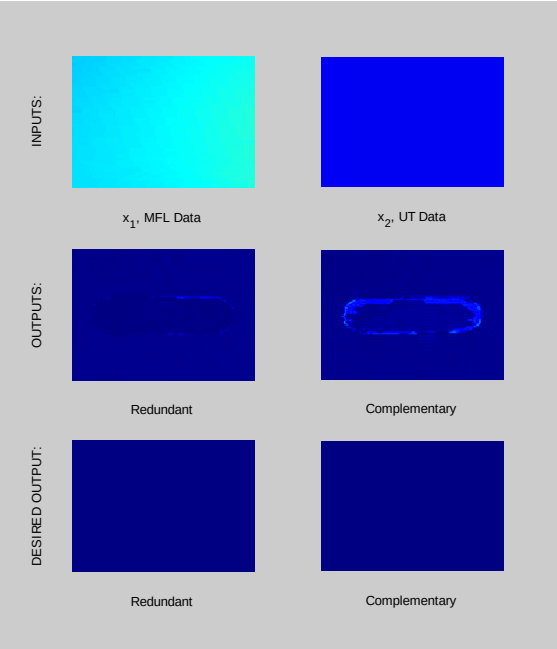

(a) Specimen 00a

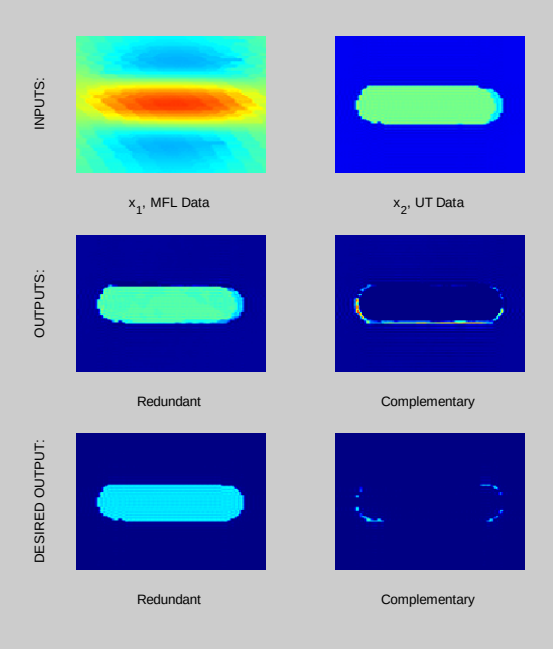

(b) Specimen 03a

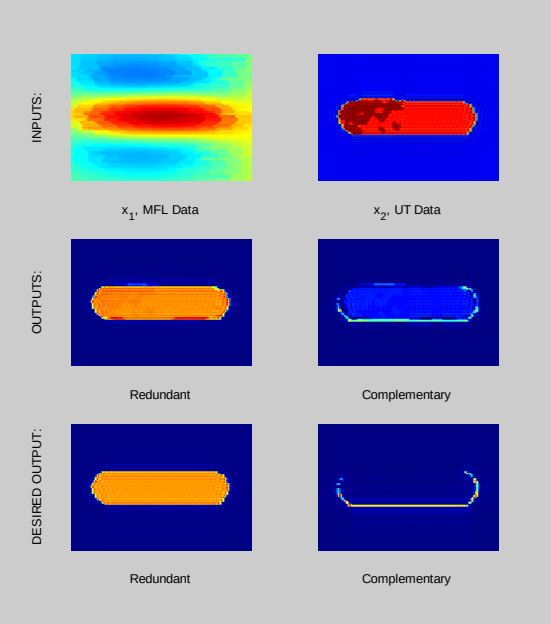

(c) Specimen 02a

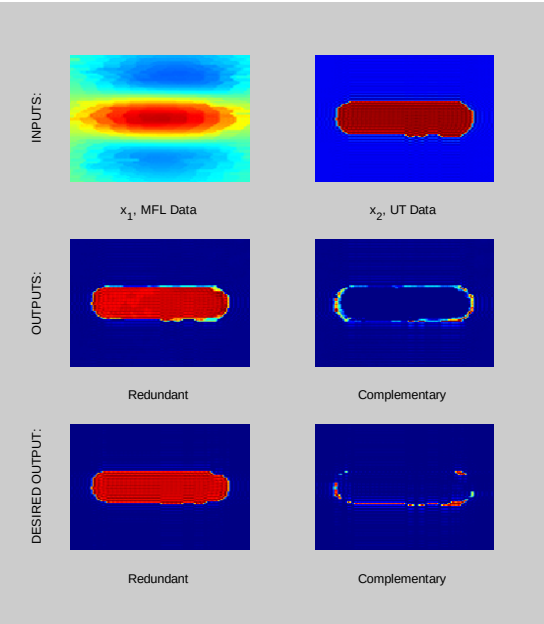

(d) Specimen 01a

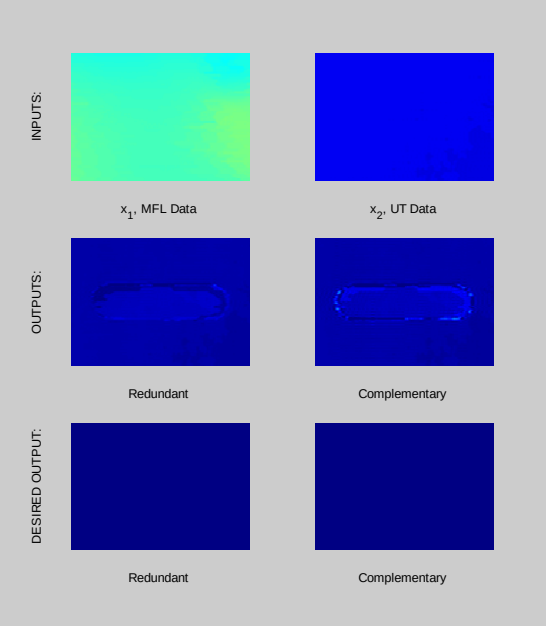

(e) Specimen 10a

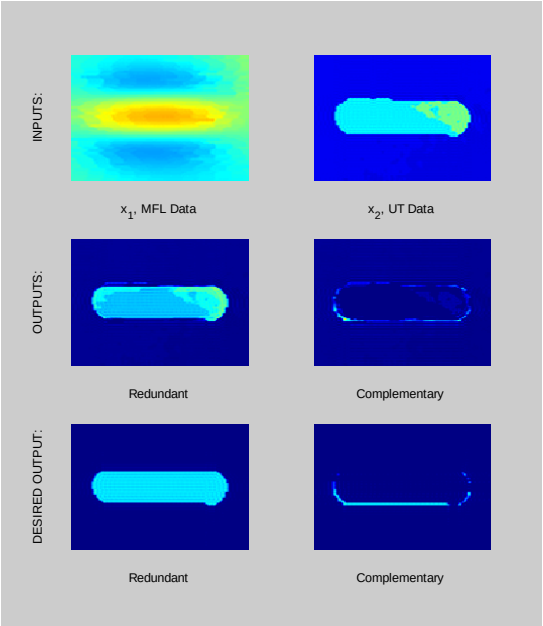

(f) Specimen 13a

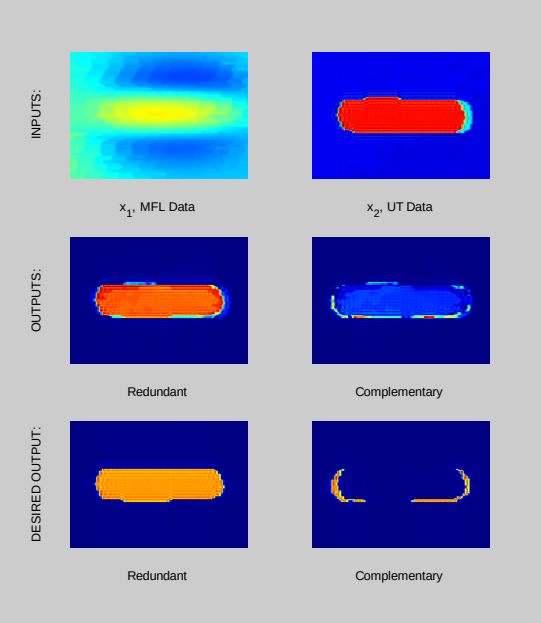

(g) Specimen 12a

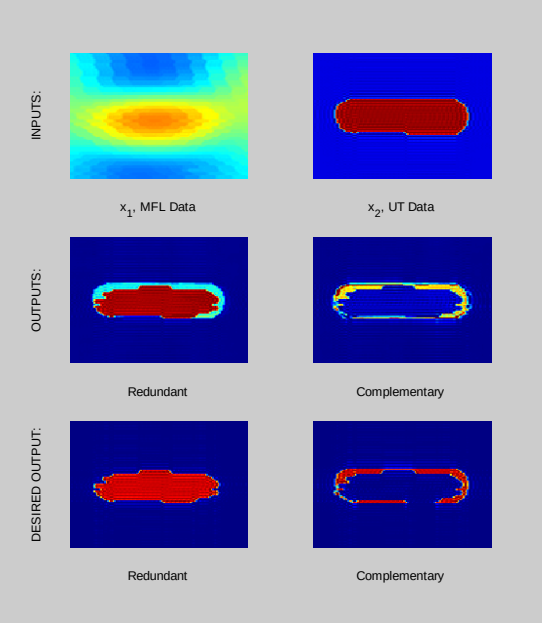

(h) Specimen 11a

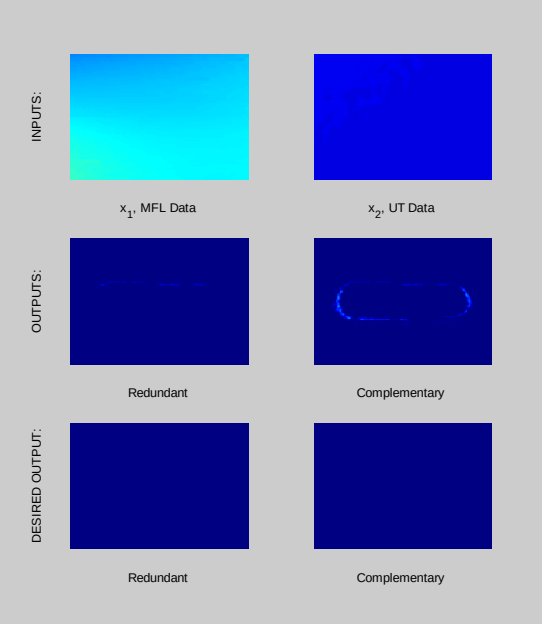

(i) Specimen 20a

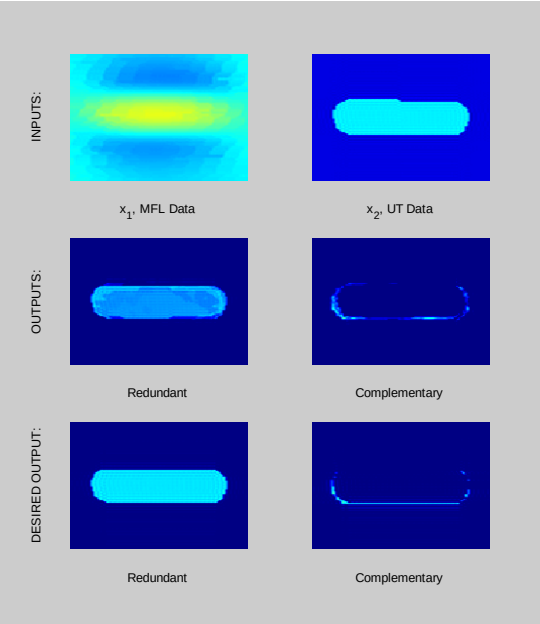

(j) Specimen 23a

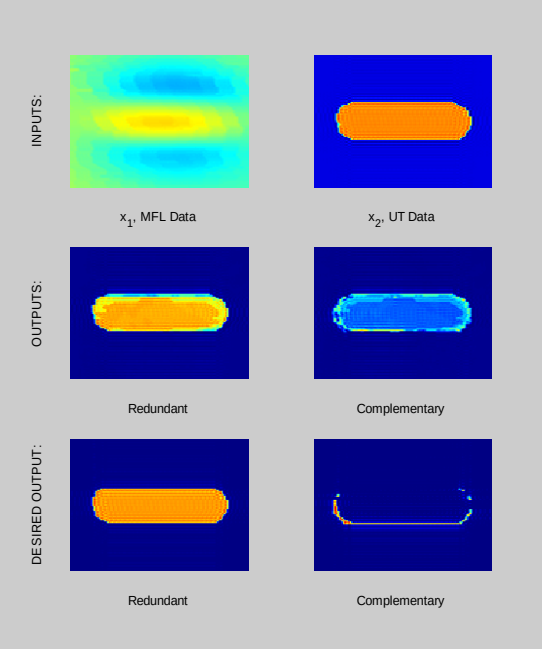

(k) Specimen 22a

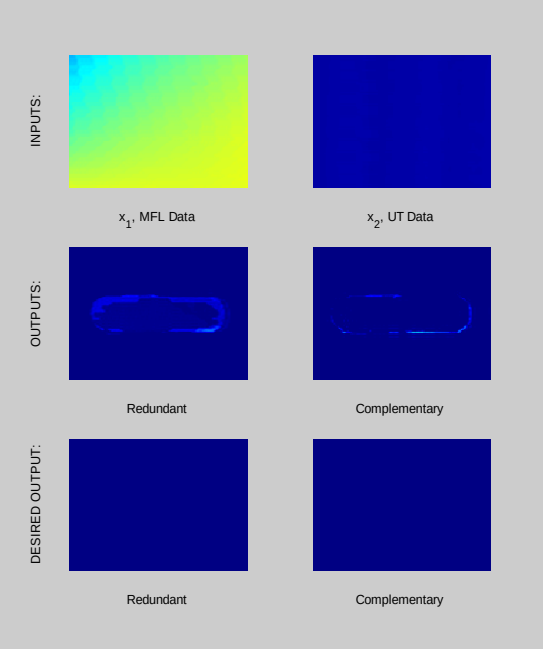

(l) Specimen 00b

Trial 1: UT & MFL Results (cont.)

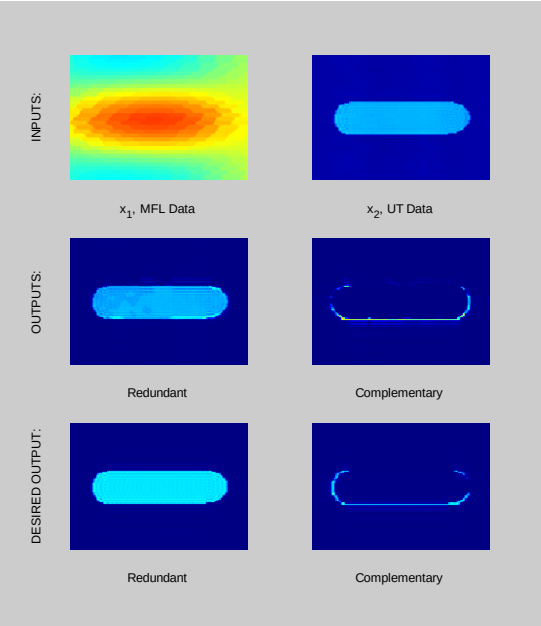

(m) Specimen 03b

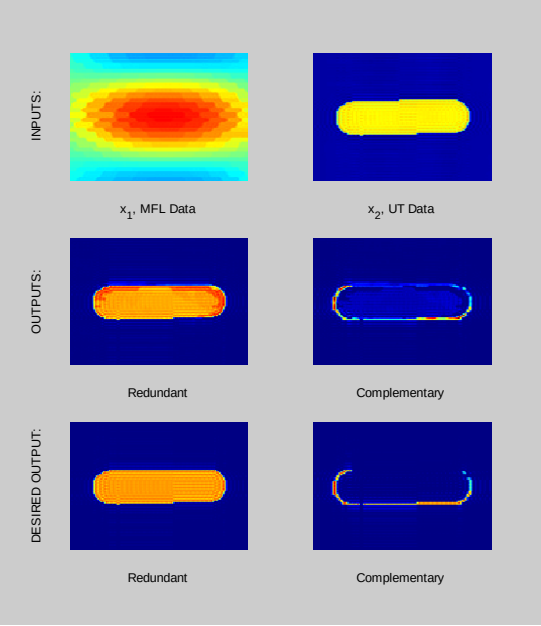

(n) Specimen 02b

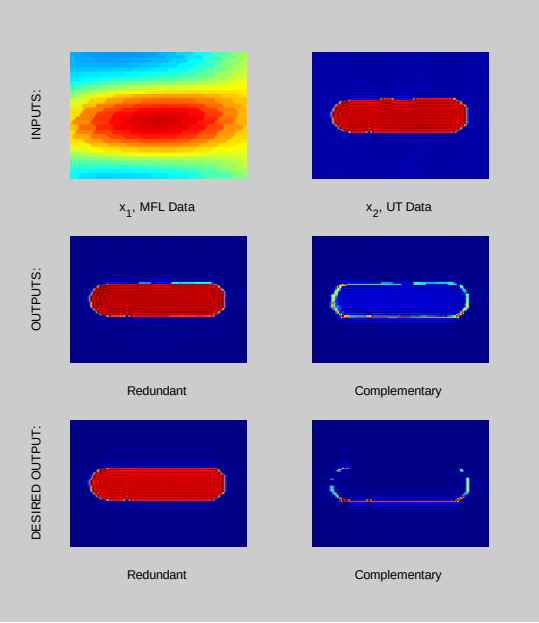

(o) Specimen 01b

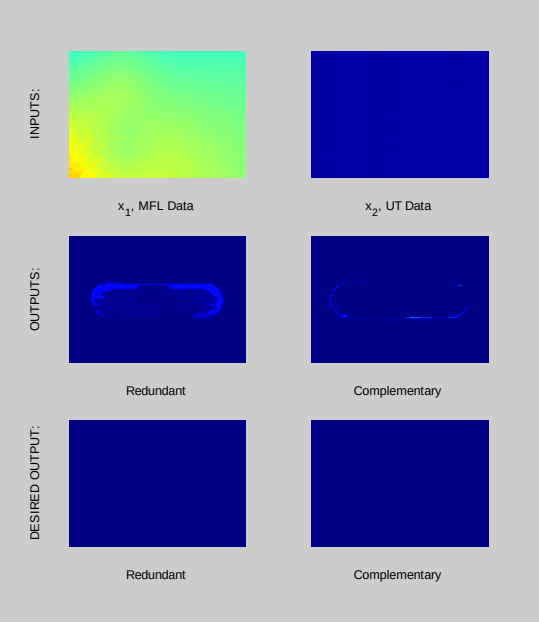

(p) Specimen 10b

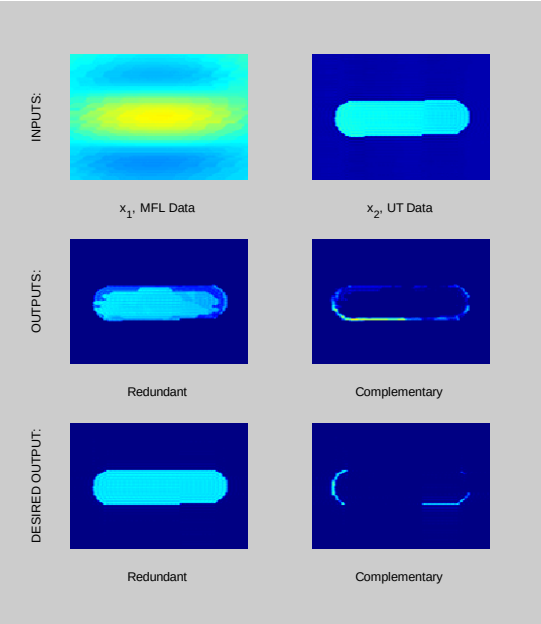

(q) Specimen 13b

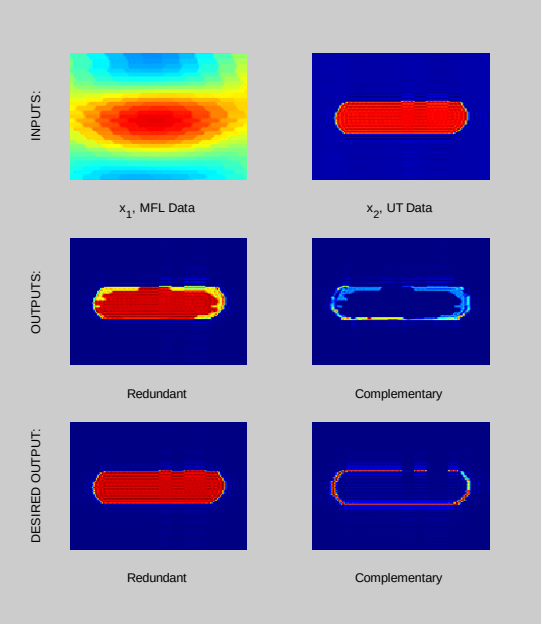

(r) Specimen 11b

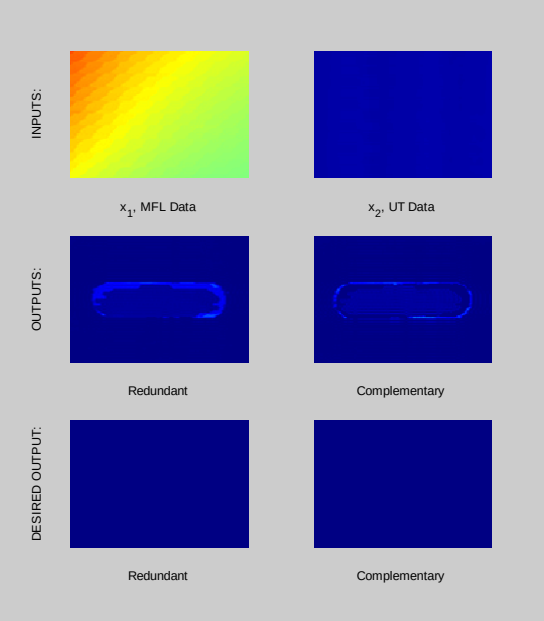

(s) Specimen 20b

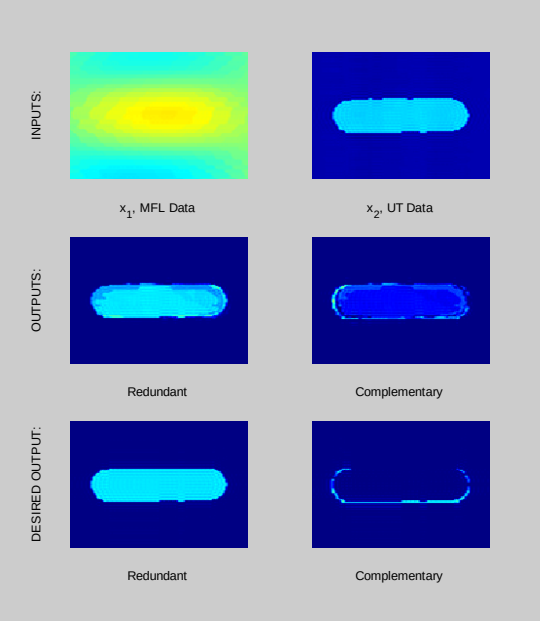

(t) Specimen 23b

Trial 1: UT & MFL Results (cont.)

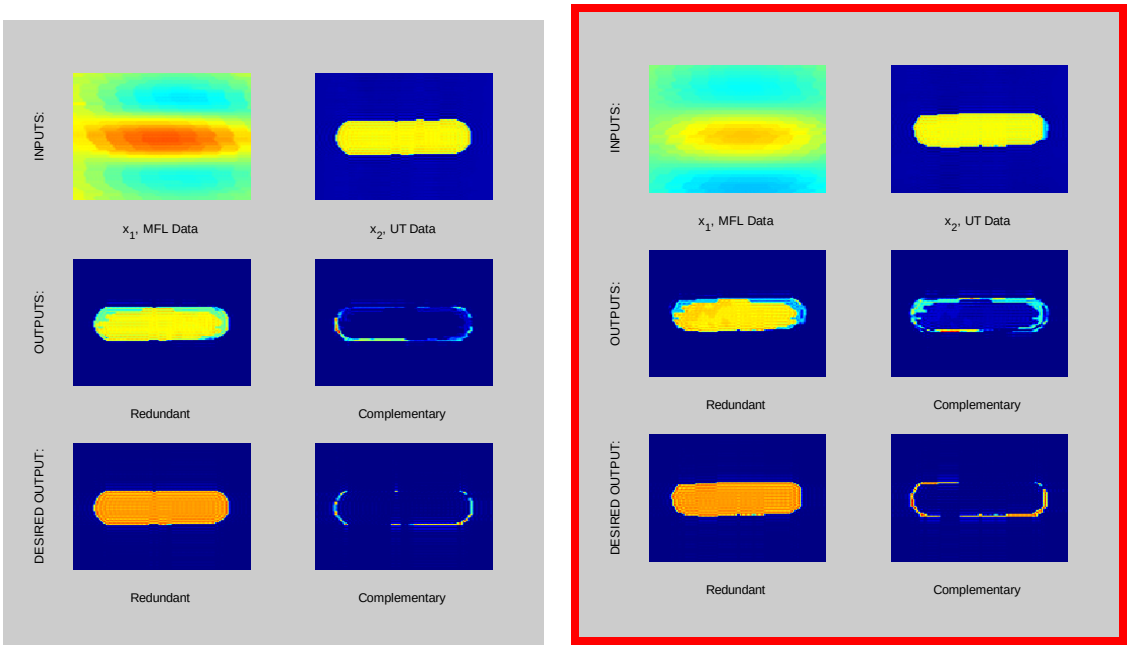

(u) Specimen 22b **(v) Specimen 01a**

Figure 23: UT & MFL Combination Trial 1

Training Data: (a) – (u); Test Data: (v)

The following observation can be made based on the data fusion results. There exists significant agreement between the predicted and desired redundant and complementary defect depth related information for all instances of training data – this indicates that the information provided to the neural network is distinct and the resulting matrices are non-singular; and is clearly visible especially the UT and MFL data combinations. The poorest performance occurs for MFL and thermal image data combinations – this is to be expected since MFL images exhibit "blooming" and cannot precisely identify the edges of the defect. This situation is worsened for thermal images where the shallowest defects are barely visible.

The homogeneous data fusion results shown are summarized in the Figures 24, 25 and 26 for purposes of comparison. In analyzing the results, the mean squared error (MSE) is used as a measure of the difference between images, because it measures how far an estimator is from what it is trying to estimate. A lower MSE indicates predicted images that are more similar to the desired output than images with a higher MSE. In analyzing the training data, the MSE between the desired training output and the actual, or predicted, training output may be analyzed. In analyzing testing results, the MSE between the desired output and the actual, or predicted, testing output may be analyzed. The MSE is useful as a relative performance measure to

compare different data sets – its use as an absolute measure of algorithm performance is limited. The mean squared error difference between the predicted and desired fused images for both redundant and complementary information, for test and training data bases is shown. The following observations can be made:

1. Over all three trials, the combination UT and MFL images produces the lowest MSE for both redundant and complementary information. This is to be expected, since quantity of information related to the geometry and location of the defect is present in the following NDE methods in decreasing order: UT, MFL, thermal imaging and AE.
2. For all three NDE data fusion combination, the lowest MSE was obtained in Trial 1, where the maximum amount of training data was present. This allowed the neural network data fusion algorithm to accurately interpolate instances of test data. The exact opposite is true of Trial 3.
3. For almost every data fusion combination and trial number, the redundant information extraction algorithm produced a lower MSE then the complementary information extraction algorithm. This is believed to be the result of the redundant training images containing more overall information then the corresponding complementary images.
4. Overall, the algorithm's predicted results matched the desired output values. The total average of the MSE for all combinations of test data was only 0.0201. Very few outputs did not meet the expectations due to poor input data for that test case. All the test data outputs are highlighted in red, where for the most part, the test data shows excellent results.

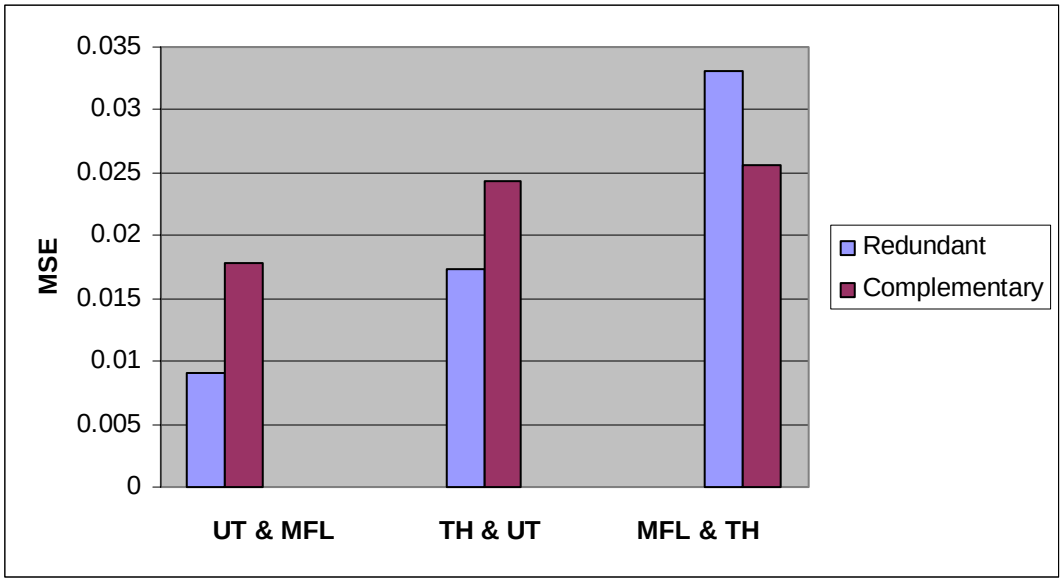

Figure 24: MSE plot of test data in Trial 1 for homogeneous data fusion.

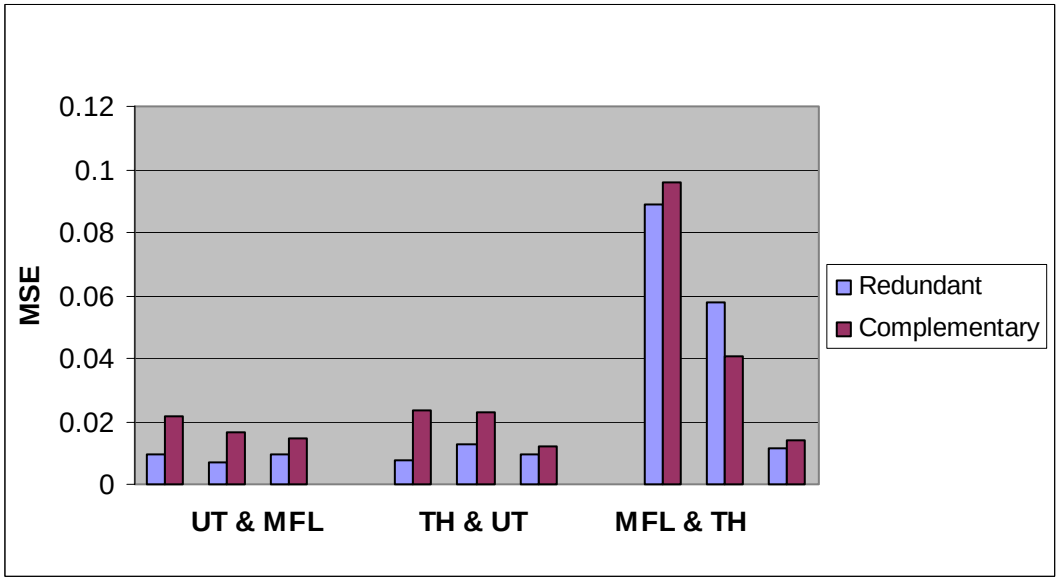

Figure 25: MSE plot of test data in Trial 2 for homogeneous data fusion.

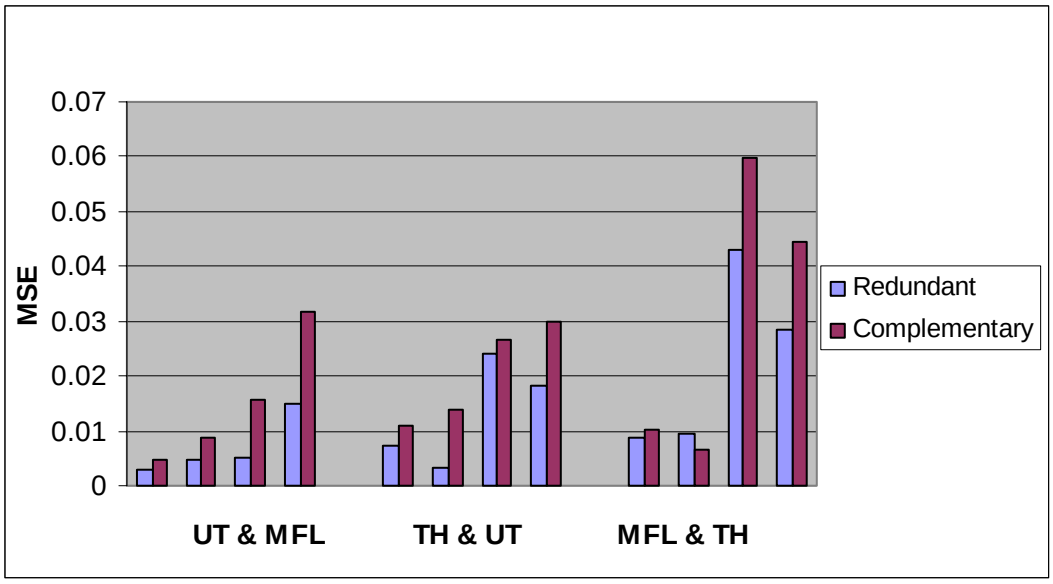

Figure 26: MSE plot of test data in Trial 3 for homogeneous data fusion.

Heterogeneous Training and Test Datasets

The heterogeneous redundant and complementary data fusion combination process was performed on ultrasonic and acoustic emission data taken of test specimen suite 2. Since only six data instances were available for training and testing purposes only two trials were performed. Trials 1 and 2 seen in Table 9 and 10 show the division of training and test data.

Table 9: Trial 1 training and test dataset.

Specimen #	Type	Plate Thickness (in)	Indication	Crack Depth (in)
Uni08	Uniaxial	0.5	SCC	0.08
Uni16	Uniaxial	0.5	SCC	0.16
Uni32	Uniaxial	0.5	SCC	0.32
Bi08	Biaxial	0.5	SCC	0.08
Bi16	Biaxial	0.5	SCC	0.16
Bi32	Biaxial	0.5	SCC	0.32

Training data Test data

Table 10: Trial 2 training and test dataset.

Uni08	Uniaxial	0.5	SCC	0.08
Uni16	Uniaxial	0.5	SCC	0.16
Uni32	Uniaxial	0.5	SCC	0.32
Bi08	Biaxial	0.5	SCC	0.08
Bi16	Biaxial	0.5	SCC	0.16
Bi32	Biaxial	0.5	SCC	0.32

Acoustic Emission & Ultrasound Data Fusion Results

Trial 1: AE & UT Results

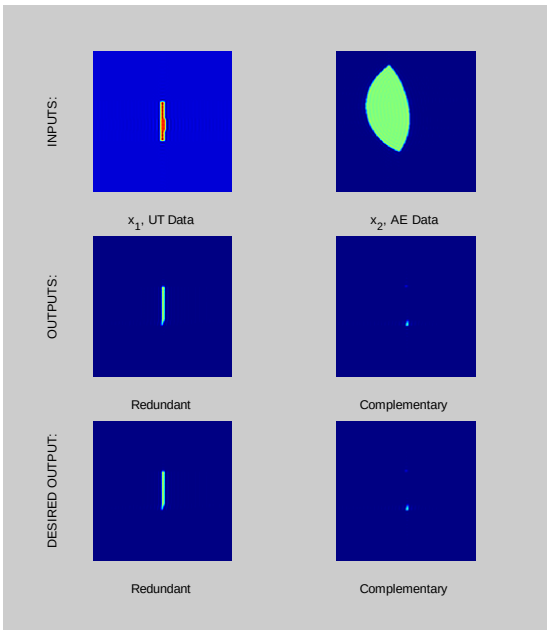

(a)

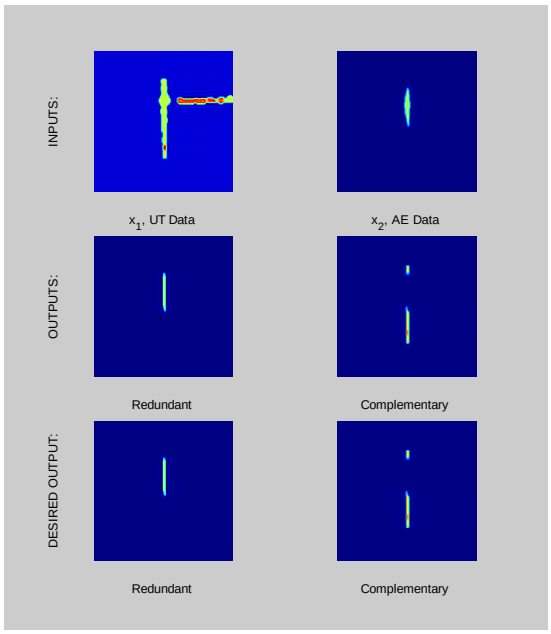

(b)

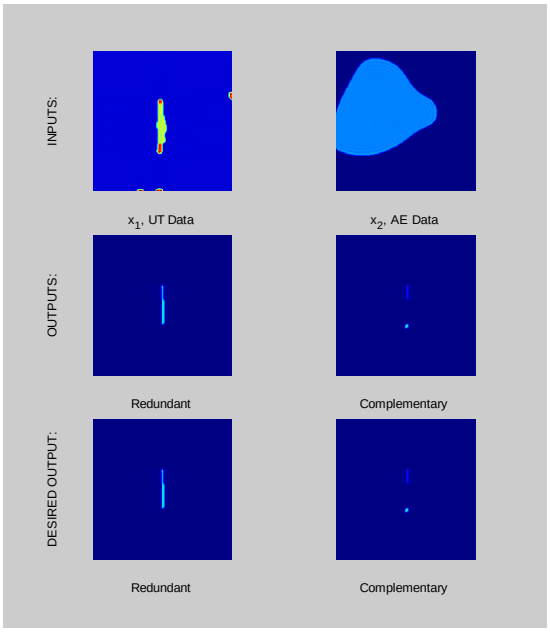

(c)

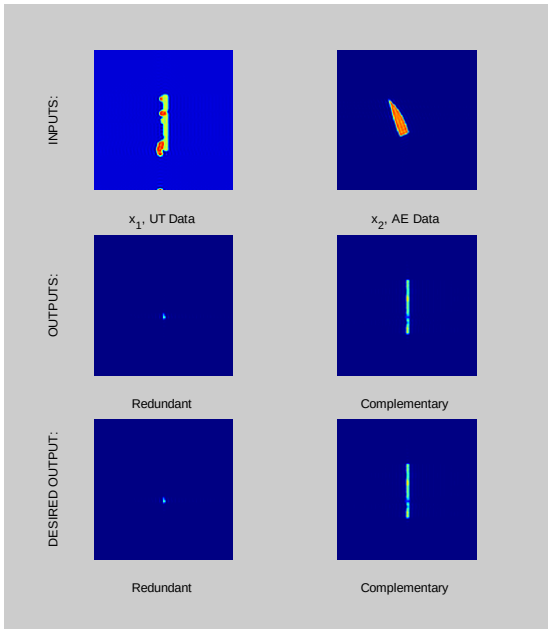

(d)

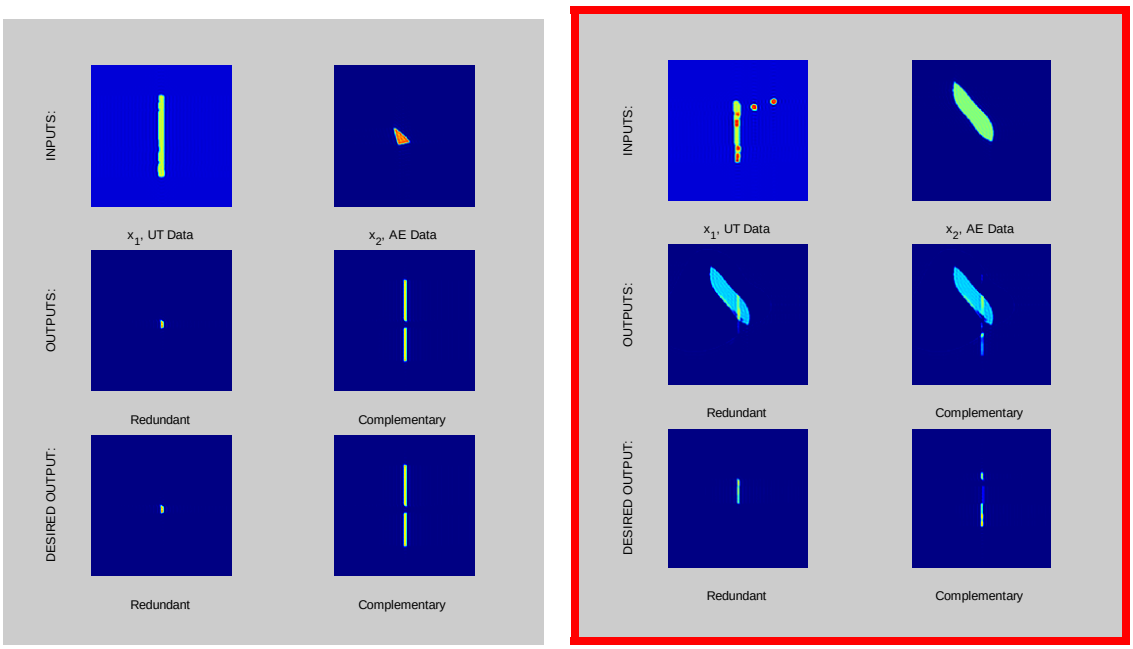

(e) (f)

Figure 27: AE & UT Combination Trial 1.

Training Data: (a) – (e); Test Data: (f)

The results from the acoustic emission and ultrasound combination show that both Trials 1 and 2 provided very good training data outputs with an average training output MSE of 2.86 x 10^{-8}. This indicates that the network was trained well and ready for testing. The subsequent test results are summarized in Figures 28 and 29 where the MSE of test outputs of Trial 1 for redundant and complementary portions are 0.0144 and 0.0156, respectively. The MSE of test outputs of Trial 2 for redundant and complementary in uniaxial are 0.0121 and 0.0133, respectively. The MSE of test outputs of Trial 2 for redundant and complementary in biaxial are 0.0187 and 0.0204, respectively. In both cases the algorithm made an effort to extract the desired information and suppress the unwanted information with a limited amount of training and test data. Although it appears that the heterogeneous data fusion produced better results (lower MSE) than the homogeneous data fusion, with a greatly increased data set, it is expected the heterogeneous data fusion method will exhibit poorer performance. That is, as more data is used for training the heterogeneous network, it is expected that the MSE of testing results will begin to rise to levels closer to those error levels seen in the homogeneous network testing results. This is because the heterogeneous data was pre-processed using a Parzen windows technique to generate an equivalent homogeneous data set, before being fused with other homogeneous data. The accuracy of the resulting data fusion is critically dependent on the accuracy of the pre-processing.

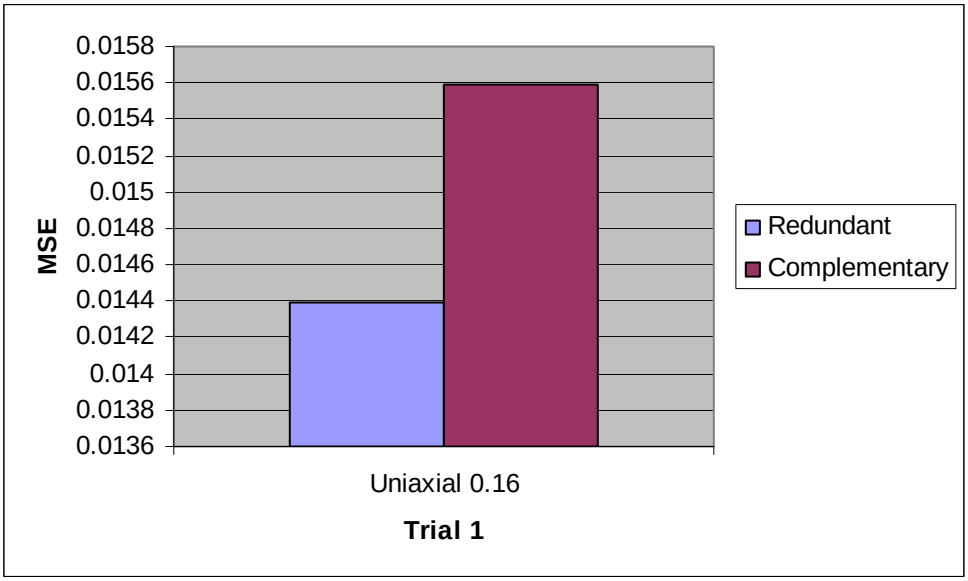

Figure 28: MSE plot of Trial 1 for heterogeneous data fusion.

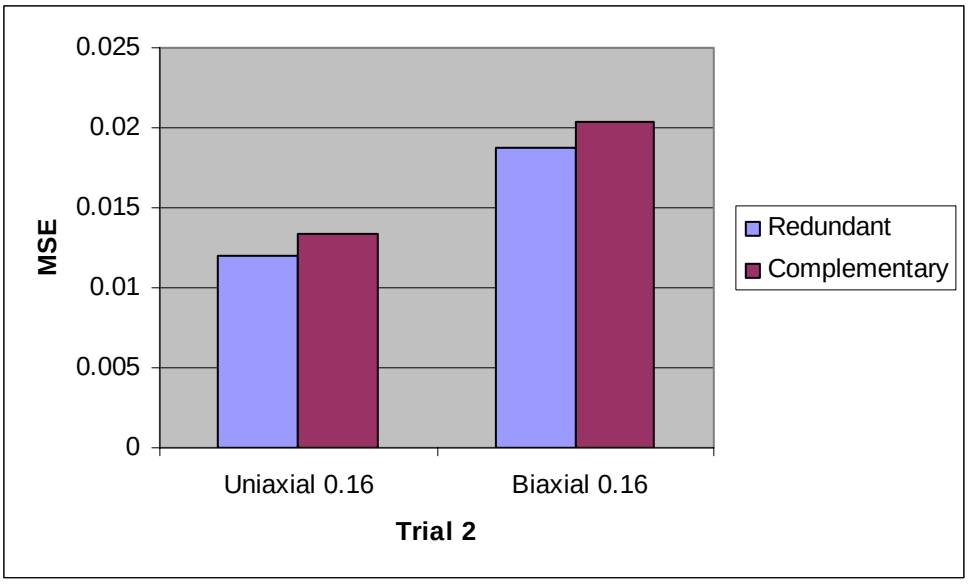

Figure 29: MSE plot of Trial 2 for heterogeneous data fusion.

Task 5.0 – Recommendations for Effective Data Management

The following worlds were created to implement the procedure as described in the previous section. The Fakespace ImmersaDesk R2, a semi-immersive display system, was the projection system used. The system includes head tracking and a tracked navigation wand. VRCO's vGeo software was used to create the virtual worlds and drive the display system.

Graphical

First, a component library was created. The library included a pipeline anchor, check valve, ball valve, T-section, tap, weld, sleeve, flange, and straight length of pipe. The graphical components were modeled and assembled using SolidWorks. All models were converted to virtual reality modeling language (VRML) files and imported into vGeo. Figure 30 shows three sections of a pipeline network, each having a different set of components.

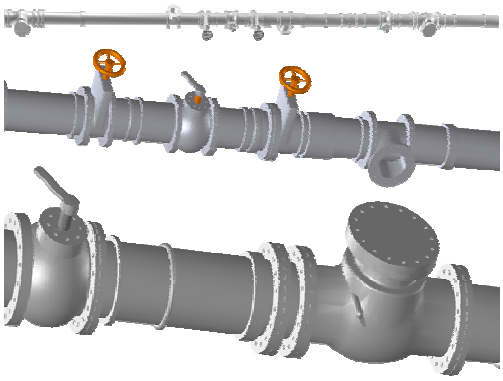

Figure 30: Pipeline sections that are composed of various library components.

Although this particular assembly was done prior to integration, it is possible to import each piece individually and create the pipeline network interactively.

ESRI's AcrMap was used to obtain certain geographical features. The software generates two-dimensional maps that can be extruded to a third dimension using ESRI's add-on package, 3-D Analyst. Files can then be imported into the virtual world as VRML files. Alternately, two-dimensional pictures can be imported into the virtual reality system. A third dimension, if desired, can then be extrapolated within vGeo. When GIS data is imported as a VRML file, the entire file is one group of data. When imported separately, each portion of data can be turned on and off in the immersive display.

Measurement and Functional

A suite of test specimens was created in order to obtain the NDE signatures from the various testing modalities. The specimens were tested using MFL, UT and thermal imaging – these have been described in previous reports. The results of the measurements were then integrated using virtual reality. The figures below show the results obtained using each of the testing methods.

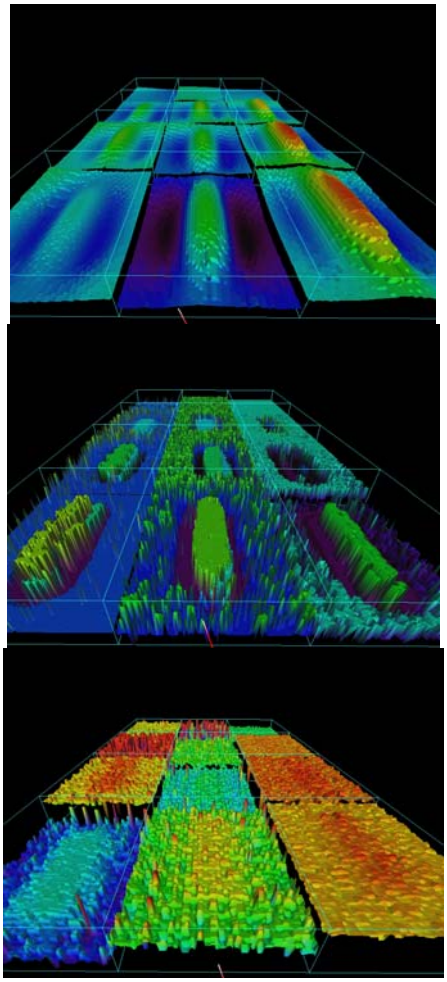

Figure 31: MFL, UT, and thermal images from the inspection of corrosion pits displayed in VR.

MFL flux data for the pipe section depicted in Figure 30 was obtained from a pig with 83 sensors around the circumference. The complete set of data for each sensor is represented by one column of data; the measurement of all 83 sensors for a particular distance measurement is represented by each row. This tabular data was then projected onto an irregularly shaped grid. After the circumferential grid was constructed, the grid was distended proportional to the magnitude of the flux observed at each sensor. This is illustrated in Figure 32.

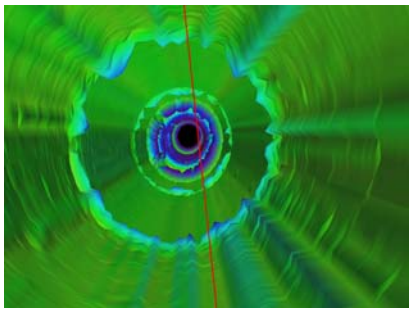

Figure 32: MFL pigging data inside a pipeline.

This information was also fed into a neural network. The ANN classified the flux signatures as one of the component model pieces. The classification results can simply be overlaid onto of the actual flux data. Figure 33 illustrates the integration of the measured data and the predicted classification result.

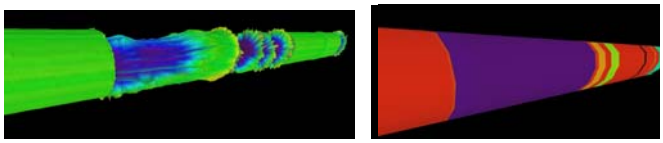

Figure 33: MFL image obtained from a section of pipe and the corresponding color-coded neural net classifications.

Integration

There are an infinite number of combinations that can be used to represent the various data modalities in a virtual world. In order to view the MFL, UT, and thermal imaging data, color mapped topologies were used. The data from Figure 3 was displayed together to investigate the three data sets at the same time. Figure 34 shows how the aggregate data is integrated.

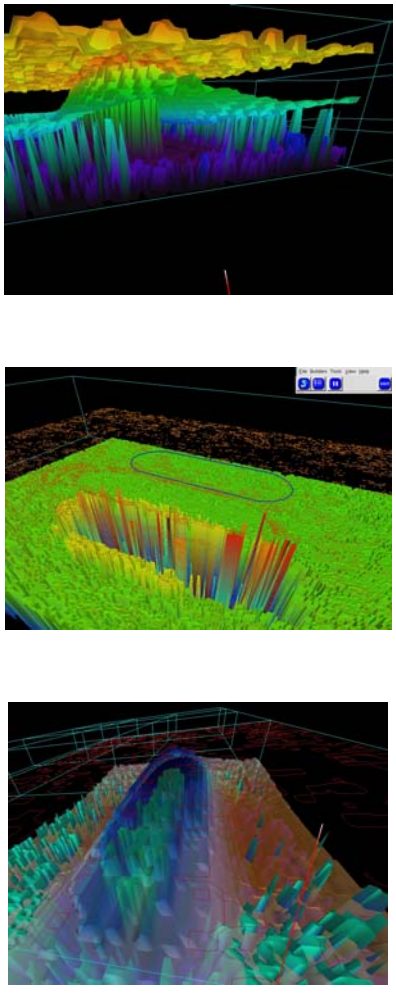

Figure 34: Various representations of MFL, UT, and thermal data sets integrated in a virtual world.

Contour slices can also be used instead of surface representations to analyze the data. Graphical representations can also be used for reference. Figure 34 shows UT data surface, a thermal contour, and a graphical contour used for reference; also a UT topology, a MFL transparent topology and a thermal contour. The same integration procedures used on the test specimen data was used on the component MFL data. A pipeline network was created and the MFL data was superimposed onto it. Figure 35 illustrates the integration for these two data types.

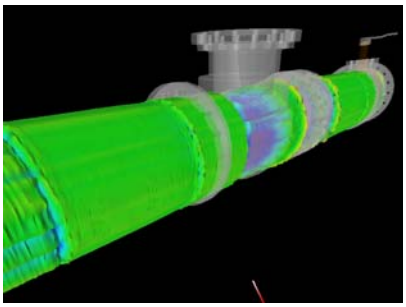

Figure 35: MFL data registered onto the graphical pipe representation.

Similarly, a pipeline network was created using less detailed components to save graphical memory. The pipeline network was then registered inside of a virtual world. The location information was conveyed through a grid, topography, and simulated GIS data. The integrated world is shown in Figure 36.

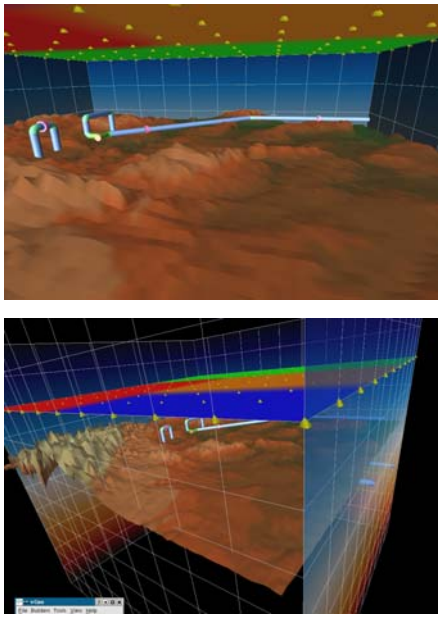

Figure 36: A view of an integrated environment for a pipeline network.

Conclusion

The principal contributions of this research project and the conclusions drawn from the work are listed below:

1. *The design and development of data fusion algorithms for the prediction of specific information fusion measures – redundancy and complementarity* – geometric transformations in combination with radial basis function networks and Parzen windows density estimation techniques have been used.
2. *The application of the data fusion algorithms to accurately and confidently predict the varying depth profile of surface-breaking pipe wall defects in a gas transmission pipeline* – combinations of UT, MFL, thermal imaging and AE NDE data have been fused to predict defect depths in the range of 0.01" – 0.03" for pipe-wall specimens of thicknesses 5/16" – 1/2". The average MSE between the predicted and desired values for the training data for all the combinations is 0.0028 and for the testing data for all combinations is 0.0201.
3. *The demonstration of the algorithms ability to fuse data from multiple homogeneous and heterogeneous sensors* – redundant and complementary information related to the location and size of a pipe-wall defect was predicted using homogeneous data combinations that include UT-MFL, UT-thermal imaging and MFL-thermal imaging; the heterogeneous data combination includes UT-AE.
4. *Research and development partnerships* – Rowan University has established a research partnership with RTD Quality Services, USA based out of Houston, Texas and through their contacts with TransCanada Pipelines. Attempts were made to obtain field inspection data – a sufficient quantity was not available for a comprehensive field validation of the methods developed as part of this research project.
5. *Development of a framework for multi-sensor data visualization in a virtual reality (VR) platform.* An immersive, interactive and navigable VR data fusion environment was defined and created, consisting of (a) graphical data, (b) measurement data, and (c) functional data. The framework was demonstrated using multi-sensor data obtained during the in-line inspection of a section of a gas transmission pipeline. Graphical models of the pipeline components were displayed in addition to MFL / UT inspection signals, neural network predictions of pipeline condition, and the geographic location of the

pipeline network. The technique allows the inspection vendor to rapidly sift through hundreds of miles of pipeline inspection data and zero-in on features of interest and suggest appropriate remediation measures, if required.

Virtual reality environments show considerable promise for the integration of multi-sensor data. The system allows a user to rapidly sift through large and complex data sets to isolate features of interest. Additionally, the VR environment has the ability to evolve as a function of both system data and user input. The use of data integration and evolution empowers the user to evaluate scenarios to make informed decisions.

References

[1] S. Mandayam, L. Udpa, S. S. Udpa and W. Lord, "Invariance transformations for magnetic flux leakage signals," *IEEE Transactions on Magnetics*, Vol. 32, No. 3, pp. 1577-1580, May 1996.

[2] S. Haykin, *Neural Networks - A Comprehensive Foundation*, Second Edition, Prentice Hall, Upper Saddle River, New Jersey, 1999.

[3] R. Polikar, et. al., "Learn++: An incremental learning algorithm for supervised neural networks," *IEEE Trans onactions Sytems., Man and Cybernetics (C), Special Issue on Knowledge Management*, 31:4, pp. 497-508, 2001.

[4] R. Duda, P. Hart and D. Stork, *Pattern Classification*, John Wiley & Sons, Inc. 2001.

[5] Linda G. Shapiro and George C. Stockman, *Computer Vision*, Prentice Hall, 2001.

[6] Mel Slater, Anthony Steed and Yiorgos Chrysanthou, *Computer Graphics and Virtual Environment*, Addison Wesley, 2002.

[7] T. Hong, *A Virtual Environment for Displaying Gas Transmission Pipeline NDE Data*, M.S. Thesis, Iowa State University, 1997.

[8] Martijn J. Schuemie, Peter Van Der Straaten, Merel Krijn and Charles A.P.G Van Der Mast. "Research on presence in virtual reality: A survey," *CyberPsychology & Behavior* 2001; 4(2): 183-201.

[9] Andries van Dam, Andrews Forsberg, David Laidlaw, Joseph La Viola and Rosemary Simpson, "Immersive VR for scientific visualization: A progress report," *IEEE Computer Graphics and Applications*, November / December 2000: 26-52.

List of Acronyms and Abbreviations

AE Acoustic emission

ANN Artificial Neural Network

DCT Discrete cosine transform

FEM Finite element method

MFL Magnetic flux leakage

MLP Multilayer perceptron

NDE Nondestructive evaluation

PSI Pounds per square inch

RBF Radial basis function

SCC Stress corrosion cracking

UT Ultrasonic testing

VR Virtual Reality